



Limb darkening and exoplanets: testing stellar model atmospheres and identifying biases in transit parameters

Néstor Espinoza^{1,2★} and Andrés Jordán^{1,2★}

¹Millennium Institute of Astrophysics, Vicuña Mackenna 4860, Santiago, Chile

²Instituto de Astrofísica, Pontificia Universidad Católica de Chile, Vicuña Mackenna 4860, Santiago, Chile

Accepted 2015 April 1. Received 2015 March 26; in original form 2015 February 17

ABSTRACT

Limb darkening is fundamental in determining transit light-curve shapes, and is typically modelled by a variety of laws that parametrize the intensity profile of the star that is being transited. Confronted with a transit light curve, some authors fix the parameters of these laws, the so-called limb darkening coefficients (LDCs), while others prefer to let them float in the light-curve fitting procedure. Which of these is the best strategy, however, is still unclear, as well as how and by how much each of these can bias the retrieved transit parameters. In this work we attempt to clarify those points by first recalculating these LDCs, comparing them to measured values from *Kepler* transit light curves using an algorithm that takes into account uncertainties in both the geometry of the transit and the parameters of the stellar host. We show there are significant departures from predicted model values, suggesting that our understanding of limb darkening still needs to improve. Then, we show through simulations that if one uses the quadratic limb darkening law to parametrize limb darkening, fixing and fitting the LDCs can lead to significant biases – up to ~ 3 and ~ 1 per cent in R_p/R_* , respectively – which are important for several confirmed and candidate exoplanets. We conclude that, in this case, the best approach is to let the LDCs be free in the fitting procedure. Strategies to avoid biases in data from present and future missions involving high precision measurements of transit parameters are described.

Key words: stars: atmospheres.

1 INTRODUCTION

It has been known since the first observations of our Sun’s surface that its observed intensity decreases towards the limb. This effect, termed limb darkening, crucially affects the shape of the transit signature a planet imprints in the observed stellar flux when passing in front of its host star. In practice, limb darkening is parametrized by laws which depend on $\mu = \cos(\theta)$, where θ is the angle between the line of sight and the normal to a given point of the stellar surface. Some of the most widely used limb darkening laws in exoplanet transit light-curve fitting are given by

$$\frac{I(\mu)}{I(1)} = 1 - a(1 - \mu) \quad (\text{the linear law}),$$

$$\frac{I(\mu)}{I(1)} = 1 - u_1(1 - \mu) - u_2(1 - \mu)^2 \quad (\text{quadratic law}),$$

$$\frac{I(\mu)}{I(1)} = 1 - \sum_{n=1}^4 c_n(1 - \mu^{n/2}) \quad (\text{non-linear law}).$$

The non-linear law has as a special case the square-root law proposed by Díaz-Cordovéz & Giménez (1992), which is obtained by setting $c_3 = c_4 = 0$, and the variant, three-parameter law, introduced by Sing et al. (2009), with $c_1 = 0$.

The laws listed above do not include all the parametrizations available for limb darkening. Klingsmith & Sobieski (1970), for example, introduced the logarithmic law for early-type stars, which is given by

$$\frac{I(\mu)}{I(1)} = 1 - l_1(1 - \mu) - l_2\mu \ln \mu,$$

while Claret & Hauschildt (2003) introduced an exponential law given by

$$\frac{I(\mu)}{I(1)} = 1 - e_1(1 - \mu) - e_2/(1 - e^\mu),$$

but these laws are less used for transit fitting in practice, mainly due to their complex forms which are harder to deal with computationally and are not implemented in the most widely used transit modelling codes to date (Mandel & Agol 2002; Eastman, Gaudi & Agol 2013; see, however, Abubekrov & Gostev 2013; Kjurkchieva et al. 2013).

★ E-mail: nsespino@uc.cl (NS); ajordan@astro.puc.cl (AJ)

Confronted with measurements of an exoplanetary transit, observers usually model the effects of limb darkening by either fitting the limb darkening coefficients (LDCs) of a given law or fixing some (or all) of them using tabulated values (see e.g. Sing 2010; Claret & Bloemen 2011 for some recent tables using the *Kepler* bandpass). However, exactly which strategy is optimal, and in which situations, is still unclear. Previous works (e.g. Csizmadia et al. 2013; Müller et al. 2013) have discussed this issue focusing on the uncertainty introduced on the parameters retrieved from transit observations but, to our knowledge, no study has yet addressed the potential bias introduced by them. Such study is called for as such biases could be limiting (1) the instruments currently obtaining high precision photometry like *Kepler*, (2) exoplanet population studies which by definition are based on averaging out random errors but not systematic ones (e.g. Schlaufman 2015) and/or (3) techniques that require high precision measurements like transmission spectroscopy. Studying the biases introduced by the treatment of limb darkening and whether or not they are significant is the main aim of this work.

The sources of potential biases introduced by assuming a given limb darkening law can be separated in four. One issue is the differences in the tabulated values of the LDCs, which are large even when the same model stellar atmospheres are used. For example, Csizmadia et al. (2013) have shown that the differences between different approaches at tabulating LDCs for the quadratic law with the ATLAS9 (Kurucz 1979) stellar atmosphere models can be as high as 20 per cent, which if incorporated in the modelling can lead to significant increases in the uncertainties of the retrieved transit parameters. The second issue is the fact that, as shown by Howarth (2011), LDCs obtained directly from the intensity profiles cannot be compared directly to coefficients observed in transit photometry due to the fact that the optimization procedures are different in each setting. This in turn implies that using LDCs obtained from an intensity profile of the star as inputs in transit photometry should lead to biases in the retrieved transit parameters. The third issue is related to model complexity: we usually model limb darkening, which in models is best represented by the non-linear law, with low-order laws such as the quadratic law. Finally, the fourth issue, and perhaps the most complicated to tackle, is the fact that we still do not know with certainty if available models do a good job at reproducing real intensity profiles of stars.

The paper is organized as follows. In Section 2 we detail our methodology for obtaining LDCs from ATLAS9 (Kurucz 1979) and PHOENIX (Husser et al. 2013) stellar model atmospheres, and compare our results with the literature in order to try understand the discrepancy between previously published tables. In Section 3 we compare our model LDCs to *Kepler* estimates for a sample of stars, taking in consideration the effects mentioned by Howarth (2011), and compare the performance of the ATLAS and PHOENIX models at predicting the observed limb darkening effect. In Section 4 we explore the biases introduced on different transit parameters by fixing or fitting the LDCs. Section 5 presents a discussion of our results and Section 6 the conclusions of our work.

2 FITTING LIMB DARKENING MODELS

The fitting of the limb darkening laws to intensity profiles obtained from stellar model atmospheres is, in principle, a relatively straightforward procedure. Given a normalized response function for a given telescope/detector $S_\lambda(\lambda)$ (e.g. $\int S_\lambda(\lambda) d\lambda = 1$, although the normalization does not really matter in practice for the calculation of LDCs), one must integrate the specific intensity $I_\lambda(\lambda, \mu)$ at

each angle $\mu_i = \cos(\theta_i)$ multiplied by the response function, i.e.

$$I(\mu_i) = \int_{\lambda_1}^{\lambda_2} I_\lambda(\lambda, \mu_i) S_\lambda(\lambda) d\lambda, \quad (1)$$

where λ_1 and λ_2 define the wavelength limits of the band. This gives the observed (by the instrument) intensity, which can then be fitted by any of the laws cited earlier after normalizing by $I(1)$. Of course, for CCDs, the recorded quantity are photons and therefore we have to divide the integrand in equation (1) by hc/λ , where h is Planck constant and c is the speed of light.

In this work we make use of two widely used model intensity libraries to calculate LDCs: the ATLAS9 model atmospheres, available from Robert L. Kurucz's webpage¹ and the 1D PHOENIX model atmospheres (Husser et al. 2013). These models differ both in the geometry used to solve the stellar atmosphere (with ATLAS models using a plane-parallel approximation and the PHOENIX models using a spherically symmetric atmosphere), and on the actual physics used on each of them (see e.g. Plez 2011, for a short up-to-date discussion on this matter), so a difference between the LDCs computed from both models is expected. We will derive and compare LDCs from these stellar atmosphere models using the *Kepler* high-resolution response function² in order to compare our results with those in the literature.

2.1 Fitting limb darkening laws with the ATLAS models

We first note that the ATLAS intensities are given per unit frequency and not per unit wavelength, so a c/λ^2 term has to be added in equation (1), and so the integral in this equation now reads

$$I(\mu_i) = \int_{\lambda_1}^{\lambda_2} \left(I_\nu(\lambda, \mu_i) \frac{c}{\lambda^2} \frac{\lambda}{hc} \right) S_\lambda(\lambda) d\lambda,$$

where the limits of integration, $\lambda_1 = 348$ nm and $\lambda_2 = 970$ nm are, in our case, the first and last wavelengths present on the *Kepler* response function. We recall, however, that in order to fit the laws cited in the Introduction what we want is the intensity normalized by $I(1)$, i.e.

$$\frac{I(\mu_i)}{I(1)} = \frac{\int_{\lambda_1}^{\lambda_2} I_\nu(\lambda, \mu_i) S_\lambda(\lambda) / \lambda d\lambda}{\int_{\lambda_1}^{\lambda_2} I_\nu(\lambda, 1) S_\lambda(\lambda) / \lambda d\lambda}. \quad (2)$$

After using numerical integration and interpolation to perform these integrals, the resulting normalized intensity profiles were fitted by a least-squares procedure using two different approaches in order to compare our results with previous works. The first approach was to fit all the angles for the non-linear law, while fitting only intensities at $\mu \geq 0.05$ for the rest of the laws, a procedure followed by Sing (2010, hereafter S10). The second approach was to fit to 100- μ points obtained by interpolating the 17 angles given by the ATLAS models³ in a linear grid from $\mu = 0.01$ to 1.0 in 0.01 steps using a cubic spline, a procedure followed by Claret & Bloemen (2011, hereafter CB11).⁴

¹ <http://kurucz.harvard.edu/grids.html>

² http://keplergo.arc.nasa.gov/kepler_response_hires1.txt

³ At first sight, fitting to 100 points that have been interpolated from a set of only 17 points given by the models seems to lack any justification. We show in what follows that there is a rationale for this procedure and that there is a well-defined criterion under which this procedure gives better results.

⁴ We will use S10 and CB11 to refer both to the papers and the methodologies assumed in those works to determine the LDCs.

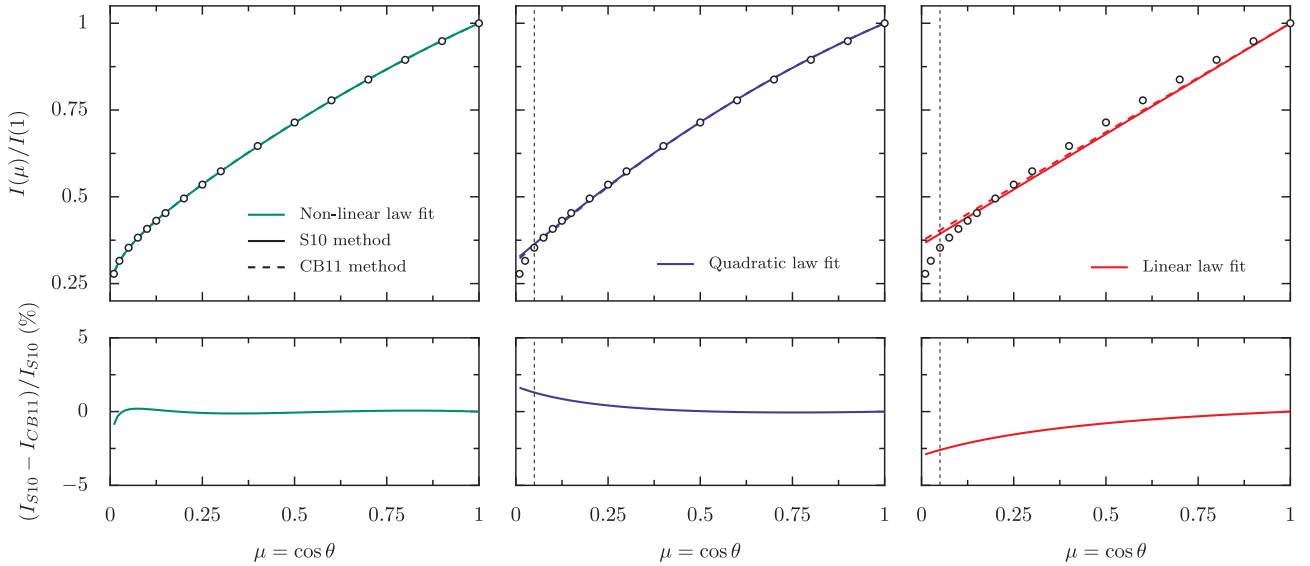


Figure 1. ATLAS stellar intensity profile obtained for the *Kepler* bandpass for a G5V-type star with solar metallicity (white points), with the coloured lines showing fits to the most popular limb darkening laws. In the upper panel, solid lines correspond to fits obtained following the method of S10, while the dashed lines correspond to fits obtained by following the method of CB11 (note these overlap in the leftmost panels). The lower panel shows the (percentual) difference between these fits. The vertical dashed black line marks $\mu = 0.05$ (see text).

We note that, because the coefficients are linear with respect to the parameters in all of the laws considered, the least-squares solutions are unique and therefore have analytic solutions given a set of intensities and angles. The exact solution, outlined in Appendix A, was used to perform the least-square fits. Fig. 1 shows the intensity profiles for a G5V star of solar metallicity (i.e. with an effective temperature of $T_{\text{eff}} = 5500$, $\log g = 4.5$, $[M/H] = 0.0$ and microturbulent velocity of $v_{\text{turb}} = 2 \text{ km s}^{-1}$) where, for illustration, fits to the most popular limb darkening laws used in the literature have been plotted following the methods of S10 (solid lines) and CB11 (dashed lines). The lower panel shows the (percentual) difference between those two methods, illustrating that they actually differ by a small (but, as we will show, significant) amount, with the differences being larger for low-order laws such as the linear (with a median difference of ~ 1 per cent, reaching a ~ 2.5 per cent difference near the limb) and smaller for high-order laws like the non-linear (with a median difference of ~ 0.1 per cent, and reaching a ~ 1 per cent difference near the extreme limb). As one would expect, the difference between the methods of S10 and CB11 is more important for the low-order laws.

2.1.1 Comparing LDCs to previous results

The large panels in Fig. 2 show the LDCs u_1 and u_2 for the quadratic law, for a range of effective temperatures, T_{eff} , calculated by us using the ATLAS models for stars with solar metallicity ($[M/H] = 0.0$), $\log g = 4.5$ and $v_{\text{turb}} = 2 \text{ km s}^{-1}$ using the S10 and CB11 procedures (blue and black points), along with the same calculations made by S10⁵ (red points), and CB11 (green points). The small panels just below each large one depict the absolute difference between our values and the ones obtained by those previous studies.

Overall, it can be seen that the coefficients we calculate follow similar trends as the ones presented in previous studies, except for the region in the range $T_{\text{eff}} \approx 7500\text{--}8500$ (grey bands in Fig. 2) where both our results and the ones of CB11 show a smooth decrease in the u_1 coefficient and a smooth increase in the u_2 coefficient, while the S10 results show a sharp increase and decrease in u_1 and u_2 , respectively. We found that this is due to S10 using old versions of the ATLAS stellar atmospheres.⁶ Using those old models (available in Robert L. Kurucz’s webpage) we recover the overall shape of the coefficients presented by S10 but cannot, however, eliminate the differences between S10 and the LDCs we calculate using the S10 methods.

Despite the similarity of the overall trend, there are significant differences between the LDCs we calculate and previous studies, even though we use their methods as described in their works and the same stellar atmospheres. The differences are of the same order of magnitude (~ 10 per cent) for both coefficients of the quadratic law, with larger differences in the u_2 coefficient for cooler stars ($T_{\text{eff}} \lesssim 5000 \text{ K}$), and in the u_1 coefficient for hotter stars ($T_{\text{eff}} \gtrsim 30000 \text{ K}$). Around solar temperatures ($5000 \lesssim T_{\text{eff}} \lesssim 6000 \text{ K}$) the differences are smaller, $\sim 0.1\text{--}1$ per cent between our results and CB11, and $\sim 1\text{--}10$ per cent between our results and S10. Although we show here only the differences with the quadratic LDCs, there are very significant deviations between the coefficients of other limb darkening laws too. In particular, we note that the LDCs of the non-linear law obtained by the different methods vary widely between works and, thus, these must be used with caution. We rule out that the differences arise from different interpolation and/or integration methods by performing the same calculations in different ways and in different programming environments.

⁵ The coefficients plotted here can be found in David Sing’s webpage: http://www.astro.ex.ac.uk/people/sing/David_Sing/Limb_Darkening.html. In particular, we used the full version of table 3.

⁶ See the note on <http://kurucz.harvard.edu/grids.html>; the new models are the ones ending in *new.pck (e.g. im01k2new.pck). The old ones (e.g. im01k2.pck19) are also available on the webpage (Kurucz, private communication).

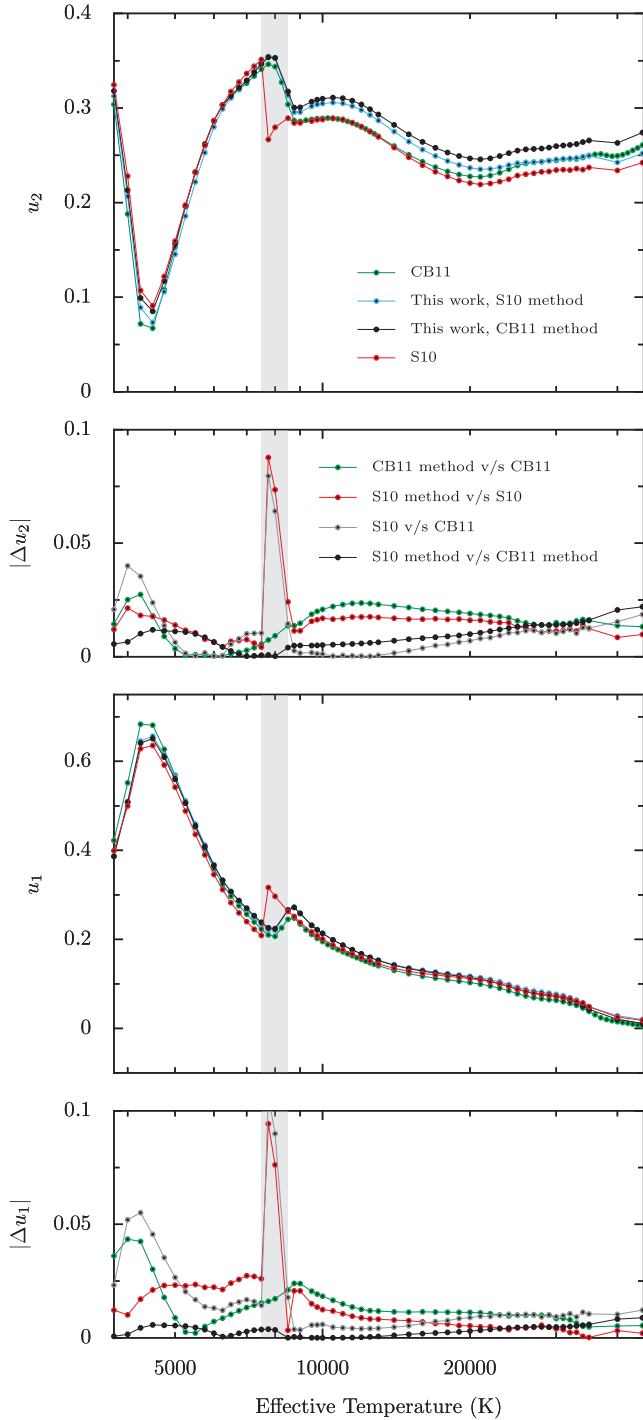


Figure 2. LDCs for the quadratic law obtained through the methods described in this work (blue and black), along with previous results by Sing (2010, red) and Claret & Bloemen (2011, green). Below each graph the absolute difference between our results and each previous study is shown, while the difference between those studies is depicted by grey points and between the S10 and CB11 methods (but with our procedures) in black points. Note the large differences in the range $T_{\text{eff}} \approx 7500\text{--}8500$ (region denoted by the grey bands) with the Sing (2010) results; this is due to Sing (2010) using old versions of the ATLAS stellar model atmospheres.

Given the results above, it is clear that the differences with previous studies do not arise from different numerical approaches but, rather, they arise either from the actual method used to obtain the LDCs (i.e. from the very definition of the integrals used to estimate the integrated intensities) or from differences in the model atmospheres used to obtain those coefficients (e.g. older versions of the ATLAS model atmospheres). Unveiling the actual source of these discrepancies is currently not feasible as the actual codes used to obtain these tables are not publicly available. We believe that in the era of high precision measurements making all details available for scrutiny in order to try understand discrepancies is fundamental. Following this logic, we provide all the codes needed to reproduce the results in this paper through [GITHUB](https://github.com/nespinoza/limb-darkening).⁷ Our codes can be used to obtain LDCs for arbitrary response functions.

2.1.2 Comparison of the methods used to fit the limb darkening laws

We now discuss which of the two fitting methods, i.e. that of S10 or that of CB11, is the most appropriate for obtaining LDCs using stellar model atmospheres, as they clearly show significant differences in Fig. 2 (black points on the small panels).

To assess which of the two methods is better, we define below a criterion that relies on an accurate analytic description of the intensity profile given by the ATLAS models. To this end, we follow Howarth (2011) and use the non-linear limb darkening law as an accurate descriptor of the intensity profile for the same stellar parameters used in Fig. 2. We note that this was done not to try to exactly reproduce the model intensity profiles but, rather, to emulate an intensity profile that is similar to the one that would be actually observed in a real stellar atmosphere. From this profile, we then obtain quadratic LDCs by sampling $N = 17$ points at the same μ values as the ones given by the ATLAS models and, with this, fit the intensity profiles using the methods of CB11 and a method similar to that of S10 (for this experiment, we choose to fit all the μ values and not only the values for which $\mu \geq 0.05$, which is the original method of S10, in order to have a fair comparison between the coefficients obtained by these two methods).

In order to assess how good the retrieved coefficients are, we obtain the ‘real’ underlying quadratic LDCs by defining them as the coefficients one would recover when sampling a very large number of points N from the (real) profile and then fitting those points with the quadratic limb darkening law. Under this definition, when $N \rightarrow \infty$, a set of ‘limiting coefficients’ should be recovered, which is the ‘real’, underlying quadratic LDCs that best fit the underlying profile. We thus take the limit as $N \rightarrow \infty$ in our least-squares procedure, imposing that the data are sampled from an underlying profile described by the non-linear law (see Appendix B). The resulting limiting coefficients for the quadratic law are given in terms of the coefficients of the underlying non-linear law by

$$\begin{aligned}
 u_{1,\text{real}} &= \lim_{N \rightarrow \infty} u_1 = \frac{12}{35}c_1 + c_2 + \frac{164}{105}c_3 + 2c_4, \\
 u_{2,\text{real}} &= \lim_{N \rightarrow \infty} u_2 = \frac{10}{21}c_1 - \frac{34}{63}c_3 - c_4.
 \end{aligned} \tag{3}$$

Fig. 3 shows the results of this experiment. The fitting method of CB11 is clearly better at obtaining the ‘real’ quadratic LDCs as we have defined them. The reason is that a cubic interpolation of the

⁷ [http://www.github.com/nespinoza/limb-darkening](https://github.com/nespinoza/limb-darkening)

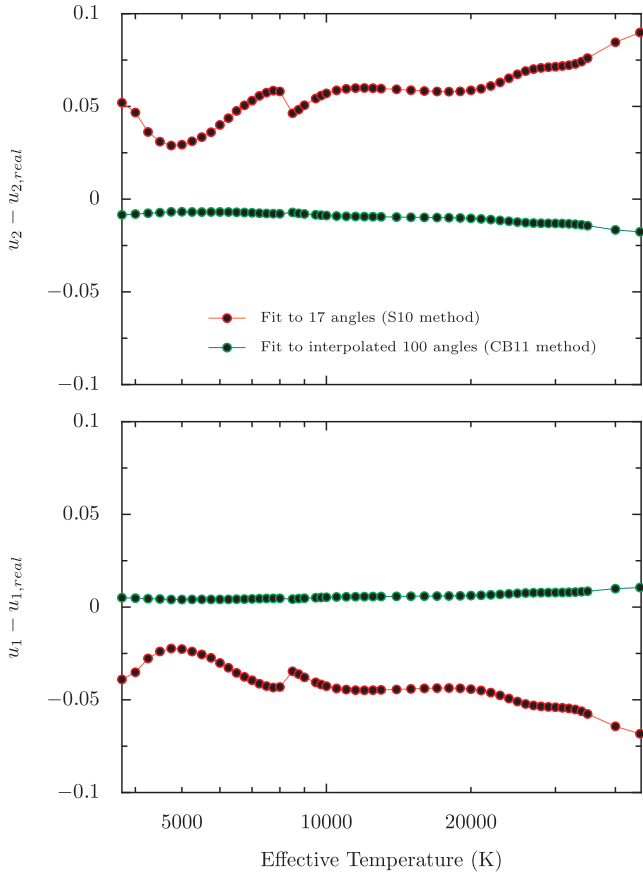


Figure 3. Differences between LDCs for the quadratic law obtained following the different methods discussed in this work (S10 in red, CB11 in green) and the ‘real’ underlying quadratic LDCs.

profile does a good job at retrieving the underlying profile (the non-linear law in the case of our experiment) and, thus, sampling points from this interpolation are very similar to sampling more points from the profile, and thus a result closer to the ‘real’ coefficients follows. It is also interesting to see that both methods fail at retrieving the ‘real’ u_1 coefficients for very hot stars. This is due to the fact that limb darkening for hotter stars is sharper than for cooler stars, changing abruptly towards the limb. Because the 17 angles given by the ATLAS models are more densely sampled close to the limb, this gives more weight to that region of the profile and thus the fit is dominated by it. Sampling uniformly across the profile, which is what the method of CB11 does, alleviates this problem and gives an overall better fit to the *whole* profile.

As a final note on this topic, we would like to note that the limiting coefficients we have introduced are the best by construction because to obtain them we use a sampling scheme that weights the whole profile uniformly. To obtain the limiting coefficients one has to make use of the non-linear LDCs, which are obtained by fitting the model intensity profiles using one of the discussed methods. However, as shown in the lower panels of Fig. 1, in the case of the non-linear law the fitting method assumed is not very relevant, producing median offsets on the order of only 0.1 per cent. Because of this, we believe that the ‘best’ quadratic LDCs that one can choose are the ‘limiting coefficients’, whose input non-linear LDCs might be obtained from either of the S10 and CB11 methods, or some other similar sampling scheme. For practical applications, we recommend using the CB11 method to fit the non-linear law to a given intensity profile and

then use the resulting coefficients to obtain the limiting coefficients according to equation (3). The codes we provide are able to carry out these calculations.

2.2 Fitting limb darkening laws to the PHOENIX models

After performing the analysis for the ATLAS stellar atmospheres, we now describe how we obtain LDCs with the PHOENIX models. The method we used is very similar to the one described for the ATLAS models, except for the fact that now we have 78 angles and, unlike ATLAS models, the intensities are given per unit wavelength. There is an additional, very important difference: unlike previous studies, we are careful in taking in consideration that the geometry of the PHOENIX models is different from that of the ATLAS models and, thus, the original intensity profiles obtained from these two model atmospheres *are not directly comparable*.

Spherically symmetric models like the PHOENIX ones extend the atmosphere by a small but important fraction ($\simeq 0.4$ per cent for older versions of PHOENIX; Aufdenberg, Ludwig & Kervella 2004) from what one usually calls the ‘stellar radius’, which is where the Rosseland mean optical depth, τ_R , satisfies $\tau_R \sim 1$. Plane-parallel model atmospheres like ATLAS, on the other hand, by definition have a very thin extended atmosphere outside the stellar radius and, therefore, have $\tau_R \sim 1$ effectively at (or very close to) the limb ($\mu = 0$). If we recall that the normalized stellar radius is given by $r = \sqrt{1 - \mu^2}$, this implies that for plane-parallel model atmospheres this outer ‘Rosseland radius’ is effectively at $r = 1$ (i.e. at $\mu = 0$), while for spherically symmetric models this radius is at $r < 1$ (i.e. at $\mu > 0$). This fact is evident when plotting the profiles of plane-parallel and spherically symmetric model atmospheres, where the PHOENIX models have a sudden decrease in intensity around $\mu \sim 0.05$ that is not present in the ATLAS profiles. This, of course, is not a fundamental difference between the models but, rather, a difference arising from the fact that these two models are defining in a different way what the ‘outer stellar radius’ or the ‘limb’ is.

One way of accounting for the different treatment of the stellar limb in spherical models is to search for the point r_{\max} at which $\tau_R \sim 1$ and redefine that point as having $\mu = 0$ *before* fitting any law to the intensity profile. This procedure allows us to have meaningful and comparable profiles between plane-parallel and spherically symmetric models. According to empirical results with the PHOENIX models, the point r_{\max} in the intensity profile can be found by searching the value at which the derivative of the intensity profile with respect to the radial intensity profile, $|dI/dr|$, is maximum (see e.g. Wittkowski, Aufdenberg & Kervella 2004). Once found, it suffices then to renormalize the radial profile by dividing by r_{\max} , thus redefining then the point at which $r = 1$ ($\mu = 0$).

Fig. 4 shows the results of applying such corrections to the PHOENIX profiles for a G5V-type star, where we have plotted the original PHOENIX profile, the ‘shifted’ version of it and the ATLAS intensity profile for comparison, which also illustrates the sudden decrease in intensity already mentioned for the PHOENIX models near $\mu = 0.05$ ($r \approx 0.9987$). The lower panel of Fig. 4 shows, for illustration, the derivative of $I(r)/I(0)$, where the maximum is indicated by the dashed line. It is evident from the upper panel of Fig. 4 that the (shifted) PHOENIX and ATLAS profiles agree for this star at the limb (which was expected because now both models are modelling the same portions of the stellar disc). It is also important to see the significant changes between the original PHOENIX profile and the corrected ones: it is clear that the original PHOENIX models were not modelling the same portions of the stellar disc as the plane-parallel models and, thus, any LDCs derived from it could not be directly

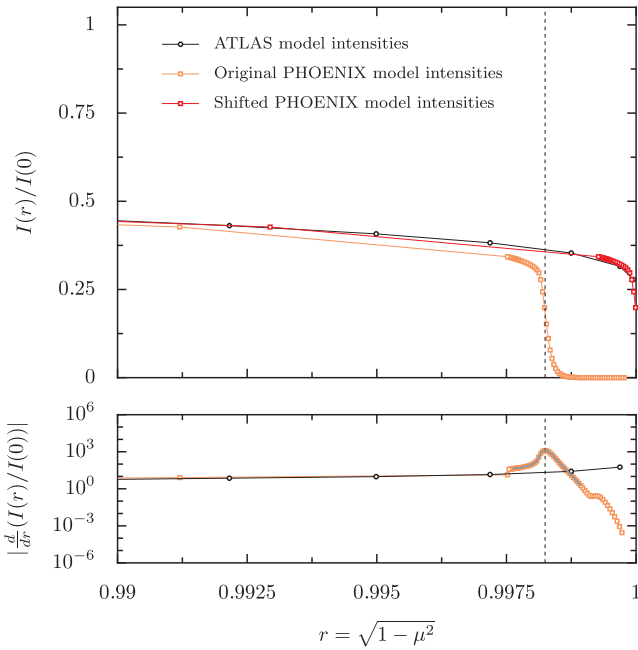


Figure 4. Close-up to the original (orange squares) and shifted (red squares) limb darkening profiles for the PHOENIX model atmosphere of a G5V-type star with solar metallicity (top) and the derivative of the intensity profile as a function of $r = \sqrt{1 - \mu^2}$ (bottom). The black circles show the ATLAS profile for comparison. The dashed line marks the value of r_{\max} found in this case.

compared to the ATLAS models. We note that this correction was not made by Claret, Hauschildt & Witte (2012, 2013, hereafter CHW) when deriving their ‘quasi-spherical’ LDCs which were obtained in order to be compared to ATLAS models, nor by Neilson & Lester (2013a, b), who also make direct comparisons between the spherical version of the ATLAS models and their plane-parallel counterparts.

Fig. 5 shows fits to the shifted PHOENIX intensity profiles to the most popular limb darkening laws used in the literature for the same model shown in Fig. 4, following the methods of S10 (solid lines) and CB11 (dashed lines). Overall, it can be seen that in the case of the PHOENIX models a larger deviation is observed between the methods used to fit the profile than for the ATLAS models (compare the lower panels between this and Fig. 1). In terms of following the profile, the CB11 method does a better job than the S10 method at following the whole profile in the case of the non-linear law. This was expected in light of our discussion in Section 2.1.2. As for the quadratic and linear law fits, both methods seem to do an adequate job at describing the profile given the low flexibility of the models.

2.2.1 Comparing LDCs with previous results

Fig. 6 shows the analogue of Fig. 2 for the quadratic LDCs obtained using the PHOENIX model atmospheres and the different methods discussed in this work, where a solar metallicity, $\log g = 4.5$ and $v_{\text{turb}} = 2 \text{ km s}^{-1}$ have been used. For comparison, the coefficients of CHW have been plotted in orange in the big panels.⁸ We can see

⁸ We note that in the models that contain the intensity profiles made available to the public by the PHOENIX team (<http://phoenix.astro.physik.uni-goettingen.de/>) there is no stellar model atmosphere for $T_{\text{eff}} = 5000 \text{ K}$, solar metallicity and $\log g = 4.5$ and, thus, we have omitted this value published by CHW in this plot.

in the figure that the overall trend for stars hotter than $\sim 4000 \text{ K}$ is similar for all cases except in the region between ~ 7500 and 9000 K , where the differences are on the order of ~ 50 per cent and for stars cooler than $\sim 4000 \text{ K}$, where the differences are larger than 100 per cent. The overall differences in the coefficients are large in comparison to the ones seen for the ATLAS models, with median differences on the order of ~ 20 per cent for both coefficients with previous works. This is mainly due to our approach using a new parametrization of the stellar disc for obtaining LDCs from spherical model atmospheres such as PHOENIX.

3 MEASURING THE LIMB-DARKENING EFFECT FROM TRANSIT LIGHT CURVES

A quantitative determination of the limb darkening effect from transit photometry requires careful thought and has been the subject of some scrutiny in recent years. For example, Csizmadia et al. (2013) have shown that the presence of uninoculated spots can lead to significant changes in the LDCs, due to the fact that a spotted stars’ intensity distribution is more complex than the simple laws given in the Introduction. Furthermore, even in the case of unspotted stars the interpretation of LDCs is subtle. Howarth (2011) showed that the geometry of the transit biases the LDCs obtained from photometry. In particular, he shows that high impact parameter transits highly bias the observed LDCs because they sample chords of the stellar surface which are closer to the limb and, thus, sample a very different part of the intensity profile as the one sampled when fitting a whole model intensity profile. This is an unavoidable problem and, therefore, LDCs obtained from high impact parameter transits are not directly comparable to the ones obtained by model intensities.

Howarth (2011) also stresses that, because the optimization processes are different when fitting an intensity profile directly from model stellar atmospheres than when fitting transit light curves, the coefficients obtained by those two procedures are not directly comparable *even if the transit is central*. This is a very important and often overlooked fact: it implies that LDCs obtained from transit light curves such as the ones obtained by Müller et al. (2013) should not be compared directly to LDCs obtained from intensity profiles derived from model stellar atmospheres. Whether this is relevant can be verified in a straightforward fashion with a simple simulation study.

(i) Select a good representation of a model intensity profile for a given set of stellar parameters derived from stellar model atmospheres, such as the non-linear limb darkening law (i.e. select a set of coefficients c_1, c_2, c_3, c_4).

(ii) Generate a (noiseless) synthetic transit light curve by feeding the chosen representation of the model intensity profile of the star and using any set of geometric parameters for the transit.

(iii) Fit this synthetic transit light curve with the same code as the one used to generate it, but now using a quadratic limb darkening law parametrization, fixing all the geometric parameters of the transit to its input values (i.e. letting just the LDCs to float).

The result of this experiment is always the same and, at first, counterintuitive: the quadratic LDCs obtained from the input model intensity profiles (obtained through e.g. the limiting coefficients obtained directly from the non-linear coefficients using equation 3), denoted in what follows as (u_1, u_2) , are *always* different from the ones obtained from the fit to the synthetic light curve, which we denote as (u_1^*, u_2^*) . Fig. 7 shows the results for this simple experiment, where we used a simulated transit light curve of a planet with a period of $P = 3 \text{ d}$, semimajor axis to stellar radius ratio $a/R_* = 0.1$,

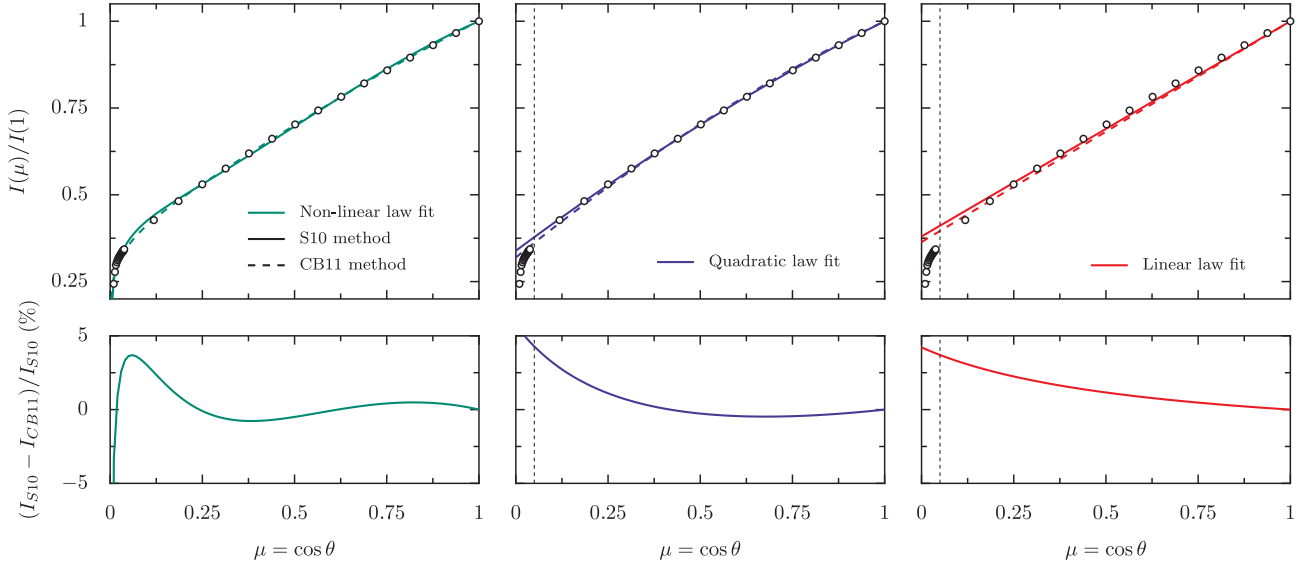


Figure 5. PHOENIX stellar intensity profile obtained for the *Kepler* bandpass for a G5V-type star with solar metallicity (white points). The panels show the same information as Fig. 1, but for the ‘shifted’ PHOENIX models.

planet-to-star radius ratio $R_p/R_* = 0.1$ on a circular ($e = 0$, $\omega = 0$), edge-on (inclination $i = \pi/2$) orbit (a typical ‘hot Jupiter’). The non-linear law LDCs (c_1 , c_2 , c_3 and c_4) were obtained for stars with $\log g = 4.5$, $[M/H] = 0.0$ and $v_{\text{turb}} = 2 \text{ km s}^{-1}$ for different temperatures of interest for exoplanet studies using the *ATLAS* models via the method of CB11 and the *Kepler* response function, and from these we derived the limiting coefficients (u_1 , u_2). The synthetic transit light curves were generated using the formalism of Mandel & Agol (2002), and the coefficients (u_1^* , u_2^*) obtained via non-linear least-squares using the Levenberg–Marquardt algorithm. 1000 points between phases -0.05 and 0.05 were generated in each simulated light curve.

From the experiment we can see that, qualitatively, the effect of observing the LDCs from photometry is to overestimate the ‘underlying’ u_1 coefficient, while the effect for the u_2 coefficient is to underestimate it. The exact mapping $(u_1, u_2) \rightarrow (u_1^*, u_2^*)$, however, is non-trivial and, thus, the comparison between LDCs obtained from transit photometry, (u_1^* , u_2^*), and from intensity profiles obtained from model stellar atmospheres, (u_1 , u_2), is also non-trivial. Furthermore, this mapping is in theory also dependent on the transit parameters, because the optimization process used to fit a transit light curve is dependent on them, although we find this dependence to be usually negligible. There is thus no simple rule to compare LDCs obtained from transit photometry with the ones obtained by model intensity profiles, and the comparison has to be done on a case-by-case basis.

3.1 Comparing photometrically obtained limb darkening coefficients to model values

In order to compare the LDCs obtained from photometric measurements to values obtained from model intensity profiles, Howarth (2011) introduced the Synthetic-Photometry/Atmosphere-Model (SPAM) algorithm, which can be summarized in three steps.

(i) Fit a transit light curve and obtain the best-fitting geometric parameters $\theta_p = \{a/R_*, R_p/R_*, e, \omega, i\}$ and best-fitting quadratic LDCs $u^f = \{u_1^f, u_2^f\}$. Obtain the stellar parameters that best rep-

resent the stellar host (e.g. via spectroscopic observations) $\theta_* = \{T_{\text{eff}}, \log g, [M/H], v_{\text{turb}}\}$.

(ii) Generate a synthetic transit light curve using the best-fitting geometrical parameters θ_p , and using an accurate representation of the model intensity profile of a star with stellar parameters θ_* , which we choose to be the non-linear law representation.

(iii) Fit the synthetic transit light curve to obtain estimates of the geometric parameters and LDCs, but now using a quadratic limb darkening law to parametrize the limb darkening effect. With this, obtain the coefficients $u^* = \{u_1^*, u_2^*\}$ which can now be directly compared to the best-fitting coefficients obtained from photometry $u^f = \{u_1^f, u_2^f\}$.

There are three very interesting things to note about this algorithm. First of all, note that this algorithm actually tests the performance of the non-linear law, i.e. of one of the best representations of the model intensity profiles that we have available, because those coefficients are the ones that are used as inputs for the algorithm which are then compared to observations. This is very interesting, as it gives us a simple tool to assess how well our model atmospheres do at predicting real, observed, intensity profiles through transit light curves. The second thing to note is that, because the non-linear law is the law being used as input, the actual method for obtaining the LDCs (i.e. flux conservation method, least-squares, etc.; see Howarth 2011, for a discussion on the differences on the obtained coefficients by those methods for the case of the quadratic law) is irrelevant in practice, because all those methods give the same coefficients in the case of the non-linear law, as shown by Claret (2000). Finally, it is very important to note that this algorithm deals mainly with the bias introduced by modelling a complex intensity profile (e.g. one following a law close to the non-linear) with a simple, two-parameter law such as the quadratic one in the transit fitting procedure. This can be verified by noting that small changes in the input non-linear LDCs (e.g. obtained from stars with similar temperatures, metallicities or gravities) give rise to larger changes between the modelled (u_i) and photometrically observed (u_i^*) LDCs than changes in the transit parameters. This means that although it is true that this algorithm deals with the bias associated with transit geometry, differences in this mapping between systems are

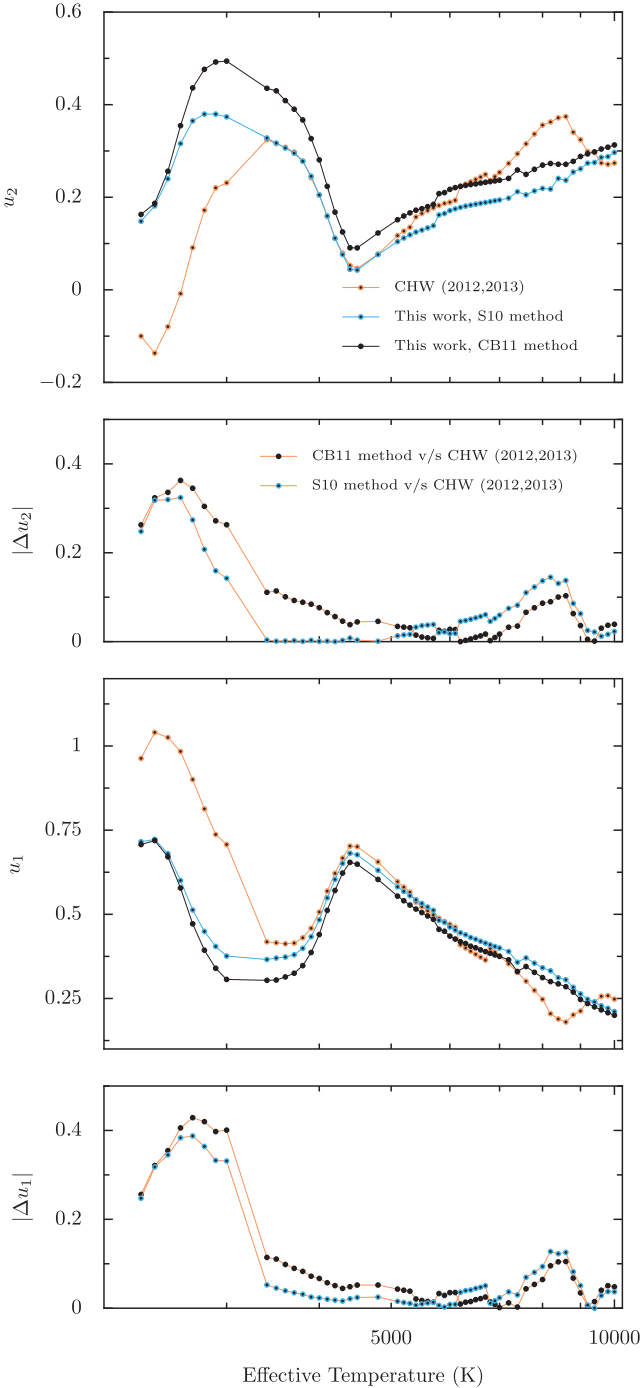


Figure 6. LDCs for the quadratic law obtained through the methods described in this work (blue and black), along with previous results by Claret et al. (2012, 2013) in orange (here we plot the coefficients obtained with the ‘quasi-spherical models’, which only fit values of $\mu \geq 0.1$ using the original PHOENIX intensity profiles); below each graph the absolute difference between our results and this previous study is shown.

currently mainly dominated by stellar parameters rather than by the actual transit geometry of a given system.

Although a big step forward in how to properly compare LDCs, the SPAM algorithm has a few shortcomings: (1) the geometric parameters are fitted in step (iii), which is inconvenient as one would want to fix them, because the objective of the algorithm is to perform

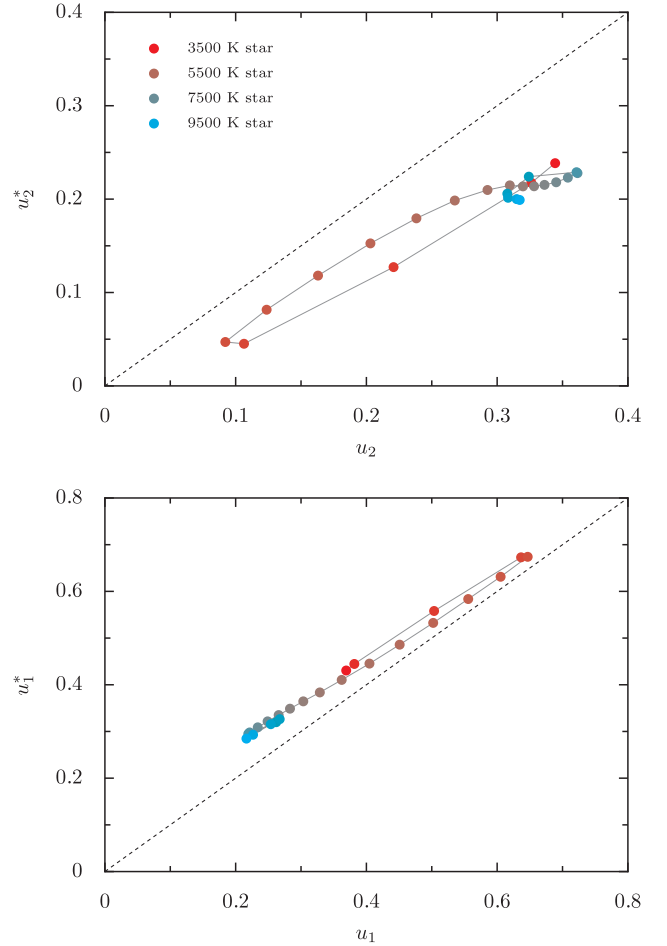


Figure 7. Simulation verifying the results of Howarth (2011), where the quadratic LDCs obtained by fitting the intensity profiles from model stellar atmospheres (u_1, u_2) for stars with $\log g = 4.5$, $[M/H] = 0.0$ and $v_{\text{turb}} = 2 \text{ km s}^{-1}$ using the ATLAS models for different temperatures are plotted against these same coefficients (u_1^*, u_2^*) obtained from synthetic transit light curves generated using these same intensity profiles. The grey line follows the temperatures of the simulated systems in increasing order for better visualization. The dashed lines depict the $u_i = u_i^*$ lines, which the points should follow if the coefficients from model intensity profiles and transit light curves were directly comparable.

the mapping $(u_1, u_2) \rightarrow (u_1^*, u_2^*)$ given a geometric setting; and (2) the algorithm does not account for uncertainties on the geometric parameters of the transit light curve, θ_p , and/or for uncertainties on the stellar parameters, θ_* . The latter is a problem because, as stated above, changes in the geometry of the transit lead to changes in the LDCs obtained from the SPAM algorithm, while errors on the stellar parameters can lead to significantly different coefficients c_1, c_2, c_3, c_4 used in step (ii) to generate the synthetic light curves. Ideally one does not obtain only best-fitting transit parameters for the geometric parameters, but also their posterior probability distribution functions (PDFs) given the data via e.g. a Markov chain Monte Carlo (MCMC) algorithm, which is information that we want to use. In most cases an MCMC approach for obtaining stellar parameters is not practical and therefore posterior distributions for these parameters are not usually available. One can still fit an ad hoc distribution to a given set of stellar parameters and their respective errors (e.g. a Gaussian for the case of a parameter with symmetric error

bars), and use that as an approximation to the posterior distribution of the stellar parameters. We propose here a modified version of the SPAM algorithm that takes into account uncertainty information. We term this algorithm Monte Carlo SPAM algorithm (MC-SPAM), and it consists of the following three steps.

(i) Fit a transit light curve and obtain the posterior PDFs given the data for the geometric parameters, i.e. $p(\theta_p|\text{data})$, with the corresponding posterior for the LDCs, $p(u^f|\text{data})$. Obtain the posterior distribution of the stellar parameters (e.g. via spectroscopic observations), $p(\theta_*|\text{data}_2)$.⁹

(ii) Draw a set of geometric parameters θ_p^d and stellar parameters θ_*^d from the posterior distribution $p(\theta_p, \theta_*|\text{data}, \text{data}_2) = p(\theta_p|\text{data})p(\theta_*|\text{data}_2)$. Apply the original SPAM algorithm to these parameters and obtain $u^{*,d} = \{u_1^{*,d}, u_2^{*,d}\}$, the SPAM LDCs for the given draw.

(iii) Repeat step (ii) to obtain a Monte Carlo sample of the model/photometric LDCs u^* , which can now be directly compared to the observed LDCs u^f .

Because in most cases no MCMC chains are available for the stellar parameters, in order to sample directly from $p(\theta_*|\text{data}_2)$, we assume independence among the stellar parameters and sample the parameters directly from their respective posterior marginal distributions, i.e.

$$p(\theta_*|\text{data}_2) = \prod_{i=1}^4 p(\theta_{i,*}|\text{data}_2),$$

where $\{\theta_{1,*}, \theta_{2,*}, \theta_{3,*}, \theta_{4,*}\} = \{T_{\text{eff}}, \log g, [\text{M}/\text{H}], v_{\text{turb}}\}$. For the modelling of the posterior marginal distributions, we assume the quoted estimates and errors come from an analysis done on a χ^2 surface, which is essentially an analysis of the likelihood $\mathcal{L}(\chi^2)$ and, thus, can be approximated by an analysis of the posterior distribution of the parameters, $p(\theta_*|\text{data}_2) \sim \mathcal{L}(\chi^2)$, if one assumes flat priors for them. In practice, we model each marginal distribution by a Gaussian in the case of symmetric error bars, where the mean is set to the best-fitting value of the parameter and its variance to the square of the error. For asymmetrical error bars, we assume a skew-normal distribution (Azzalini 1985), which is the natural choice for a ‘normal-like’ distribution with lack of symmetry. Details on the method we use to fit the parameters of this distribution given an estimate of a parameter and a set of asymmetrical error bars, as well as how to sample from the resulting distribution, are given in Appendix C. We note that although $\log g$, v_{turb} and T_{eff} are positive quantities and our treatment can in principle allow negative values, in practice, the parameter uncertainties do not allow such values to be sampled and even if they did, our algorithm is capable of detecting and discarding those values as invalid.

Our MC-SPAM algorithm is available at GitHub.¹⁰ We now use it to compare our estimates of the observed LDCs to a set of *Kepler* planets.

3.2 Comparing model to observed LDCs using *Kepler* data

Photometrically derived LDCs from fits to *Kepler* transit light curves were obtained from various sources in the literature in order to re-

trieve LDCs for stars with different parameters that host transiting planets with different geometries. Because the posterior distributions for the parameters of those systems are not published, we choose to use the same parametrization used for the stellar parameters in order to sample values given their published quantiles (i.e. in the case of symmetrical error bars we assume the posterior, marginalized distribution of each parameter is a Gaussian, while for the case of asymmetrical error bars we assume the posterior is best described by a skew-normal distribution). We note that the uncertainties associated with the transit parameters had negligible influence on the retrieved estimates of the LDCs obtained with our MC-SPAM algorithm, which were mainly dominated by the stellar parameter uncertainties.

We took data from the high signal-to-noise ratio, low impact parameter sample of Müller et al. (2013) where we additionally removed the objects that had impact parameters larger than $b = 0.5$, which were Kepler-43b ($b = 0.65$), Kepler-45b ($b = 0.6$), Kepler-7b ($b = 0.556$), Kepler-8b ($b = 0.72$), KIC 5357901b (KOI-188b; Hébrard et al. 2014, $b = 0.6$), Kepler-41b ($b = 0.54$) and Kepler-15b ($b = 0.56$). In order to be as conservative as possible, we also removed all the objects which have not been confirmed as planets to date, including Kepler-71b, for which no spectroscopic confirmation has been published so far that can rule out the possibility of it being a low-mass star, as Howell et al. (2010) can only constrain its mass to be less than $0.1 M_{\odot}$. We also remove Kepler-3b (HAT-P-11b) from our sample because its host star has been shown to have a significant amount of activity (Fraine et al. 2014) and thus the LDCs might be significantly biased (Csizmadia et al. 2013). In addition, we add Kepler-93b to our sample (Ballard et al. 2014), the recently validated Jupiter-sized planets KOI-206b and KOI-680b (Almenara et al. 2015) and, at the expense of larger errors on the estimated LDCs but in order to expand the effective temperatures sampled in this work, we also add the newly confirmed planets with low impact parameters Kepler-186f, Kepler-296f, Kepler-296e, Kepler-436b, Kepler-439b, Kepler-440b, Kepler-441b, Kepler-442b and Kepler-443b (Torres et al. 2015). Table 1 summarizes the best-fitting transit parameters for each of these planets, while Table 2 summarizes the host-star parameters. Table 3 presents both the model LDCs (u_1, u_2) and the $u^* = (u_1^*, u_2^*)$ coefficients, obtained using 1000 samples from our MC-SPAM algorithm for each target. We used both the ATLAS and PHOENIX models with the methods discussed in Section 2. A microturbulent velocity of 2 km s^{-1} was assumed for stars for which no measurement of this parameter was published.

Fig. 8 shows the published LDCs (u_1^f, u_2^f) as white points with error bars. For easier visualization, the planets have been divided into two groups: the ones with low precision (upper panels) and the other with high precision (lower panels) limb darkening measurements; note that these also separate the cooler (upper panels, $T_{\text{eff}} = 3572\text{--}5431 \text{ K}$) and the hotter ($T_{\text{eff}} = 5520\text{--}7650 \text{ K}$) stars in the sample. At the sides of each data point, the MC-SPAM results (u_1^*, u_2^*) for each system using the ATLAS models (left, blue points) and PHOENIX models (right, red points) are shown. The arrows show the changes from the median of the *model* quadratic LDCs sampled by the MC-SPAM algorithm (u_1, u_2) (i.e. the values obtained directly from the intensity profiles; in this case, they are the ‘limiting coefficients’ obtained using the non-linear law) to the median of the resulting MC-SPAM values (u_1^*, u_2^*). Fig. 9 shows the differences between the measured LDCs and the MC-SPAM values, with coloured bands indicating the 68 per cent band of the mean of those differences for the case of the ATLAS (blue bands) and PHOENIX (red bands) models. Kepler-296e was omitted from the calculation of the distribution of the mean of the differences (see below).

⁹ Note that we make explicit the fact that, in most cases, the data set used to constrain the geometric parameters of the transit and the data set used to constrain the stellar parameters are different. The algorithm does not rely on this fact, however.

¹⁰ <http://www.github.com/nespinoza/mc-spam>

Table 1. Sample of confirmed *Kepler* planets for which LDCs have been obtained.

Planet name	R_p/R_*	$i(^{\circ})$	a/R_*	e	ω	u_1^f	u_2^f	Reference
Kepler-423b	$0.12662^{+0.00029}_{-0.00028}$	$87.78^{+0.10}_{-0.11}$	$8.163^{+0.030}_{-0.034}$	0 (fixed)	0 (fixed)	$0.459^{+0.017}_{-0.017}$	$0.151^{+0.038}_{-0.035}$	Müller et al. (2013)
Kepler-77b	$0.09958^{+0.00026}_{-0.00026}$	$88.00^{+0.10}_{-0.12}$	$9.749^{+0.054}_{-0.055}$	0 (fixed)	0 (fixed)	$0.514^{+0.019}_{-0.018}$	$0.118^{+0.037}_{-0.036}$	Müller et al. (2013)
Kepler-17b	$0.13354^{+0.00017}_{-0.00019}$	$89.71^{+0.29}_{-0.13}$	$5.707^{+0.010}_{-0.008}$	0 (fixed)	0 (fixed)	$0.412^{+0.015}_{-0.015}$	$0.180^{+0.035}_{-0.032}$	Müller et al. (2013)
Kepler-6b	$0.09412^{+0.00008}_{-0.00013}$	$89.39^{+0.26}_{-0.38}$	$7.551^{+0.029}_{-0.011}$	0 (fixed)	0 (fixed)	$0.480^{+0.007}_{-0.007}$	$0.138^{+0.015}_{-0.016}$	Müller et al. (2013)
Kepler-422b	$0.09625^{+0.00025}_{-0.00022}$	$88.09^{+0.05}_{-0.06}$	$13.826^{+0.073}_{-0.076}$	0 (fixed)	0 (fixed)	$0.438^{+0.026}_{-0.024}$	$0.171^{+0.042}_{-0.047}$	Müller et al. (2013)
Kepler-12b	$0.11879^{+0.00013}_{-0.00013}$	$88.79^{+0.11}_{-0.13}$	$8.018^{+0.019}_{-0.020}$	0 (fixed)	0 (fixed)	$0.428^{+0.007}_{-0.008}$	$0.124^{+0.018}_{-0.017}$	Müller et al. (2013)
Kepler-2b	$0.07764^{+0.00004}_{-0.00004}$	$83.12^{+0.04}_{-0.05}$	$4.152^{+0.006}_{-0.006}$	0 (fixed)	0 (fixed)	$0.357^{+0.007}_{-0.007}$	$0.162^{+0.011}_{-0.012}$	Müller et al. (2013)
Kepler-5b	$0.07972^{+0.00006}_{-0.00009}$	$89.39^{+0.61}_{-0.20}$	$6.459^{+0.023}_{-0.008}$	0 (fixed)	0 (fixed)	$0.368^{+0.009}_{-0.011}$	$0.142^{+0.020}_{-0.019}$	Müller et al. (2013)
Kepler-13b	$0.08553^{+0.00007}_{-0.00007}$	$85.82^{+0.10}_{-0.12}$	$4.434^{+0.011}_{-0.010}$	0 (fixed)	0 (fixed)	$0.308^{+0.007}_{-0.007}$	$0.222^{+0.014}_{-0.013}$	Müller et al. (2013)
Kepler-93b	$0.014751^{+0.000059}_{-0.000059}$	$89.183^{+0.044}_{-0.044}$	$12.496^{+0.015}_{-0.015}$	0 (fixed)	0 (fixed)	$0.449^{+0.063}_{-0.063}$	$0.188^{+0.089}_{-0.089}$	Ballard et al. (2014)
Kepler-186f	$0.0205^{+0.0012}_{-0.0013}$	$89.96^{+0.04}_{-0.10}$	178^{+65}_{-21}	0 (fixed)	0 (fixed)	$0.70^{+0.39}_{-0.38}$	$-0.16^{+0.31}_{-0.30}$	Torres et al. (2015)
Kepler-296f	$0.0362^{+0.0022}_{-0.0018}$	$89.95^{+0.05}_{-0.12}$	137^{+34}_{-15}	0 (fixed)	0 (fixed)	$0.35^{+0.31}_{-0.32}$	$-0.01^{+0.35}_{-0.20}$	Torres et al. (2015)
Kepler-296e	$0.0297^{+0.0029}_{-0.0037}$	$89.89^{+0.11}_{-0.26}$	71^{+29}_{-10}	0 (fixed)	0 (fixed)	$1.52^{+0.32}_{-0.34}$	$-0.70^{+0.23}_{-0.27}$	Torres et al. (2015)
Kepler-436b	$0.0354^{+0.0024}_{-0.0035}$	$89.93^{+0.07}_{-0.18}$	104^{+34}_{-16}	0 (fixed)	0 (fixed)	$0.67^{+0.44}_{-0.48}$	$-0.14^{+0.38}_{-0.31}$	Torres et al. (2015)
Kepler-439b	$0.02392^{+0.00099}_{-0.00111}$	$89.95^{+0.05}_{-0.12}$	142^{+18}_{-15}	0 (fixed)	0 (fixed)	$0.39^{+0.28}_{-0.34}$	$-0.08^{+0.25}_{-0.23}$	Torres et al. (2015)
Kepler-440b	$0.03038^{+0.00112}_{-0.0027}$	$89.93^{+0.07}_{-0.18}$	$99.0^{+10.2}_{-9.4}$	0 (fixed)	0 (fixed)	$0.34^{+0.24}_{-0.23}$	$-0.05^{+0.21}_{-0.19}$	Torres et al. (2015)
Kepler-441b	$0.0280^{+0.0017}_{-0.0014}$	$89.97^{+0.03}_{-0.07}$	260^{+83}_{-31}	0 (fixed)	0 (fixed)	$0.28^{+0.27}_{-0.28}$	$-0.02^{+0.30}_{-0.20}$	Torres et al. (2015)
Kepler-442b	$0.0211^{+0.0019}_{-0.0016}$	$89.94^{+0.06}_{-0.12}$	146^{+80}_{-22}	0 (fixed)	0 (fixed)	$1.03^{+0.50}_{-0.49}$	$-0.43^{+0.32}_{-0.43}$	Torres et al. (2015)
Kepler-443b	$0.0304^{+0.0022}_{-0.0022}$	$89.94^{+0.06}_{-0.13}$	151^{+39}_{-22}	0 (fixed)	0 (fixed)	$0.65^{+0.41}_{-0.48}$	$-0.15^{+0.25}_{-0.31}$	Torres et al. (2015)
KOI-206b	$0.06590^{+0.00015}_{-0.00015}$	$89.21^{+0.52}_{-0.90}$	$6.44^{+0.62}_{-0.62}$	$0.119^{+0.079}_{-0.079}$	68^{+67}_{-36}	$0.325^{+0.022}_{-0.022}$	$0.220^{+0.045}_{-0.045}$	Almenara et al. (2015)
KOI-680b	$0.06384^{+0.00020}_{-0.00020}$	$85.51^{+0.52}_{-0.52}$	$6.35^{+0.51}_{-0.51}$	$0.114^{+0.077}_{-0.077}$	104^{+36}_{-36}	$0.374^{+0.024}_{-0.024}$	$0.180^{+0.042}_{-0.042}$	Almenara et al. (2015)

Table 2. Parameters of the host stars of each of the planets listed in Table 1.

Star name	T_{eff} (K)	$\log g$ (cgs)	[M/H] ^a	v_{turb} (km s ⁻¹)	Reference
Kepler-423	5790^{+116}_{-116}	$4.57^{+0.12}_{-0.12}$	$0.26^{+0.12}_{-0.12}$...	Endl et al. (2014)
Kepler-77	5520^{+60}_{-60}	$4.40^{+0.10}_{-0.10}$	$0.20^{+0.05}_{-0.05}$	1.8 ± 0.3	Gandolfi et al. (2013)
Kepler-17	5781^{+85}_{-85}	$4.53^{+0.12}_{-0.12}$	$0.26^{+0.10}_{-0.10}$...	Bonomo et al. (2012)
Kepler-6	5647^{+44}_{-44}	$4.236^{+0.011}_{-0.011}$	$0.34^{+0.04}_{-0.04}$...	Dunham et al. (2010)
Kepler-422	5972^{+84}_{-84}	$4.50^{+0.10}_{-0.10}$	$0.23^{+0.09}_{-0.09}$...	Endl et al. (2014)
Kepler-12	5947^{+100}_{-100}	$4.175^{+0.015}_{-0.011}$	$0.07^{+0.04}_{-0.04}$...	Fortney et al. (2011)
Kepler-2	6366^{+78}_{-80}	$4.01^{+0.01}_{-0.01}$	$0.28^{+0.11}_{-0.11}$...	Lund et al. (2014)
Kepler-5	6297^{+60}_{-60}	$3.96^{+0.10}_{-0.10}$	$0.04^{+0.06}_{-0.06}$...	Koch et al. (2010)
Kepler-13A	7650^{+250}_{-250}	$4.2^{+0.50}_{-0.50}$	$0.2^{+0.20}_{-0.20}$...	Shporer et al. (2014)
Kepler-93	5669^{+75}_{-75}	$4.470^{+0.004}_{-0.004}$	$-0.18^{+0.10}_{-0.10}$...	Ballard et al. (2014)
Kepler-186	3755^{+90}_{-90}	$4.736^{+0.020}_{-0.019}$	$-0.26^{+0.12}_{-0.12}$...	Torres et al. (2015)
Kepler-296	3572^{+80}_{-80}	$4.833^{+0.025}_{-0.041}$	$-0.12^{+0.12}_{-0.12}$...	Torres et al. (2015)
Kepler-436	4651^{+100}_{-100}	$4.619^{+0.015}_{-0.028}$	$0.01^{+0.10}_{-0.10}$...	Torres et al. (2015)
Kepler-439	5431^{+100}_{-100}	$4.514^{+0.035}_{-0.073}$	$0.02^{+0.10}_{-0.10}$...	Torres et al. (2015)
Kepler-440	4134^{+154}_{-154}	$4.706^{+0.049}_{-0.016}$	$-0.30^{+0.15}_{-0.15}$...	Torres et al. (2015)
Kepler-441	4340^{+177}_{-177}	$4.715^{+0.047}_{-0.024}$	$-0.57^{+0.18}_{-0.18}$...	Torres et al. (2015)
Kepler-442	4402^{+100}_{-100}	$4.673^{+0.018}_{-0.021}$	$-0.37^{+0.10}_{-0.10}$...	Torres et al. (2015)
Kepler-443	4723^{+100}_{-100}	$4.614^{+0.016}_{-0.029}$	$-0.01^{+0.10}_{-0.10}$...	Torres et al. (2015)
KOI-206	6360^{+140}_{-140}	$3.892^{+0.056}_{-0.056}$	$-0.01^{+0.20}_{-0.20}$...	Almenara et al. (2015)
KOI-680	6161^{+94}_{-94}	$3.613^{+0.047}_{-0.070}$	$-0.18^{+0.11}_{-0.11}$...	Almenara et al. (2015)

Note. ^aIt is assumed that [M/H] = [Fe/H].

In general, just as we observed in our simulation shown in Fig. 7, the shifts between the (u_1, u_2) and (u_1^*, u_2^*) coefficients produced by the MC-SPAM are larger for the u_2 coefficients than for the u_1 coefficients, and the effect is to correct the model underestimation

of the u_1 coefficients and the model overestimation of u_2 ; in other words, the effect of the mapping $u_1 \rightarrow u_1^*$ is to increase the value of u_1 , while the effect of the mapping $u_2 \rightarrow u_2^*$ goes in the opposite direction. As observed in Figs 8 and 9, this mapping is in general

Table 3. Results of the LDCs obtained using the MC-SPAM algorithm.

Planet name	u_1 (ATLAS)	u_2 (ATLAS)	u_1^* (ATLAS)	u_2^* (ATLAS)	u_1 (PHOENIX)	u_2 (PHOENIX)	u_1^* (PHOENIX)	u_2^* (PHOENIX)
Kepler-423b	$0.419^{+0.023}_{-0.021}$	$0.263^{+0.013}_{-0.014}$	$0.457^{+0.022}_{-0.020}$	$0.197^{+0.009}_{-0.010}$	$0.463^{+0.021}_{-0.011}$	$0.206^{+0.007}_{-0.014}$	$0.504^{+0.021}_{-0.013}$	$0.142^{+0.009}_{-0.014}$
Kepler-77b	$0.367^{+0.073}_{-0.128}$	$0.182^{+0.039}_{-0.063}$	$0.394^{+0.077}_{-0.138}$	$0.139^{+0.028}_{-0.047}$	$0.503^{+0.006}_{-0.005}$	$0.182^{+0.002}_{-0.003}$	$0.546^{+0.006}_{-0.006}$	$0.113^{+0.003}_{-0.003}$
Kepler-17b	$0.420^{+0.018}_{-0.016}$	$0.262^{+0.010}_{-0.011}$	$0.463^{+0.016}_{-0.016}$	$0.190^{+0.006}_{-0.008}$	$0.464^{+0.017}_{-0.009}$	$0.206^{+0.006}_{-0.012}$	$0.502^{+0.017}_{-0.010}$	$0.145^{+0.007}_{-0.012}$
Kepler-6b	$0.448^{+0.008}_{-0.009}$	$0.245^{+0.006}_{-0.005}$	$0.488^{+0.008}_{-0.009}$	$0.178^{+0.005}_{-0.004}$	$0.495^{+0.006}_{-0.006}$	$0.185^{+0.004}_{-0.003}$	$0.538^{+0.006}_{-0.007}$	$0.116^{+0.005}_{-0.004}$
Kepler-422b	$0.384^{+0.016}_{-0.014}$	$0.284^{+0.008}_{-0.010}$	$0.414^{+0.016}_{-0.014}$	$0.225^{+0.006}_{-0.008}$	$0.446^{+0.009}_{-0.010}$	$0.215^{+0.005}_{-0.005}$	$0.487^{+0.011}_{-0.012}$	$0.151^{+0.010}_{-0.007}$
Kepler-12b	$0.373^{+0.016}_{-0.016}$	$0.287^{+0.009}_{-0.009}$	$0.419^{+0.014}_{-0.013}$	$0.206^{+0.004}_{-0.005}$	$0.455^{+0.007}_{-0.008}$	$0.209^{+0.003}_{-0.002}$	$0.496^{+0.007}_{-0.008}$	$0.144^{+0.003}_{-0.003}$
Kepler-2b	$0.324^{+0.011}_{-0.010}$	$0.319^{+0.005}_{-0.005}$	$0.354^{+0.012}_{-0.010}$	$0.248^{+0.003}_{-0.003}$	$0.438^{+0.006}_{-0.005}$	$0.210^{+0.002}_{-0.002}$	$0.486^{+0.006}_{-0.005}$	$0.137^{+0.002}_{-0.003}$
Kepler-5b	$0.322^{+0.006}_{-0.006}$	$0.313^{+0.003}_{-0.003}$	$0.379^{+0.005}_{-0.005}$	$0.213^{+0.001}_{-0.001}$	$0.441^{+0.005}_{-0.005}$	$0.209^{+0.003}_{-0.001}$	$0.483^{+0.005}_{-0.006}$	$0.143^{+0.004}_{-0.002}$
Kepler-13b	$0.243^{+0.045}_{-0.021}$	$0.352^{+0.013}_{-0.028}$	$0.299^{+0.038}_{-0.019}$	$0.246^{+0.009}_{-0.012}$	$0.321^{+0.019}_{-0.012}$	$0.275^{+0.010}_{-0.013}$	$0.371^{+0.023}_{-0.013}$	$0.198^{+0.008}_{-0.015}$
Kepler-93b	$0.402^{+0.016}_{-0.017}$	$0.268^{+0.010}_{-0.010}$	$0.434^{+0.016}_{-0.016}$	$0.212^{+0.008}_{-0.008}$	$0.465^{+0.012}_{-0.015}$	$0.205^{+0.009}_{-0.007}$	$0.503^{+0.013}_{-0.016}$	$0.146^{+0.011}_{-0.009}$
Kepler-186f	$0.259^{+0.042}_{-0.037}$	$0.420^{+0.025}_{-0.033}$	$0.318^{+0.039}_{-0.036}$	$0.303^{+0.031}_{-0.028}$	$0.219^{+0.035}_{-0.035}$	$0.466^{+0.024}_{-0.033}$	$0.302^{+0.033}_{-0.037}$	$0.309^{+0.031}_{-0.023}$
Kepler-296f	$0.289^{+0.037}_{-0.032}$	$0.404^{+0.025}_{-0.028}$	$0.346^{+0.033}_{-0.032}$	$0.293^{+0.026}_{-0.018}$	$0.232^{+0.028}_{-0.027}$	$0.475^{+0.019}_{-0.020}$	$0.322^{+0.027}_{-0.031}$	$0.308^{+0.027}_{-0.014}$
Kepler-296e	$0.293^{+0.036}_{-0.034}$	$0.401^{+0.027}_{-0.029}$	$0.345^{+0.032}_{-0.036}$	$0.299^{+0.031}_{-0.020}$	$0.234^{+0.029}_{-0.029}$	$0.475^{+0.019}_{-0.022}$	$0.319^{+0.027}_{-0.034}$	$0.316^{+0.030}_{-0.016}$
Kepler-436b	$0.617^{+0.013}_{-0.016}$	$0.115^{+0.011}_{-0.010}$	$0.644^{+0.015}_{-0.017}$	$0.071^{+0.014}_{-0.012}$	$0.619^{+0.011}_{-0.013}$	$0.117^{+0.009}_{-0.007}$	$0.657^{+0.012}_{-0.015}$	$0.057^{+0.012}_{-0.009}$
Kepler-439b	$0.465^{+0.022}_{-0.021}$	$0.229^{+0.014}_{-0.015}$	$0.493^{+0.022}_{-0.021}$	$0.179^{+0.014}_{-0.014}$	$0.505^{+0.012}_{-0.012}$	$0.184^{+0.006}_{-0.005}$	$0.545^{+0.012}_{-0.013}$	$0.119^{+0.007}_{-0.007}$
Kepler-440b	$0.419^{+0.107}_{-0.112}$	$0.277^{+0.092}_{-0.088}$	$0.472^{+0.095}_{-0.099}$	$0.177^{+0.068}_{-0.062}$	$0.378^{+0.116}_{-0.107}$	$0.312^{+0.083}_{-0.091}$	$0.441^{+0.105}_{-0.092}$	$0.196^{+0.059}_{-0.063}$
Kepler-441b	$0.479^{+0.076}_{-0.120}$	$0.219^{+0.090}_{-0.058}$	$0.520^{+0.062}_{-0.110}$	$0.146^{+0.062}_{-0.036}$	$0.456^{+0.117}_{-0.129}$	$0.260^{+0.088}_{-0.075}$	$0.507^{+0.105}_{-0.124}$	$0.166^{+0.070}_{-0.051}$
Kepler-442b	$0.559^{+0.032}_{-0.047}$	$0.159^{+0.036}_{-0.025}$	$0.590^{+0.029}_{-0.038}$	$0.104^{+0.022}_{-0.017}$	$0.546^{+0.040}_{-0.061}$	$0.177^{+0.046}_{-0.034}$	$0.585^{+0.037}_{-0.052}$	$0.108^{+0.033}_{-0.023}$
Kepler-443b	$0.607^{+0.014}_{-0.018}$	$0.122^{+0.014}_{-0.010}$	$0.633^{+0.016}_{-0.019}$	$0.080^{+0.015}_{-0.013}$	$0.610^{+0.013}_{-0.014}$	$0.123^{+0.010}_{-0.008}$	$0.647^{+0.015}_{-0.017}$	$0.064^{+0.014}_{-0.011}$
KOI-206b	$0.315^{+0.015}_{-0.013}$	$0.315^{+0.007}_{-0.006}$	$0.370^{+0.014}_{-0.011}$	$0.215^{+0.005}_{-0.003}$	$0.440^{+0.007}_{-0.008}$	$0.209^{+0.004}_{-0.004}$	$0.483^{+0.008}_{-0.008}$	$0.140^{+0.004}_{-0.003}$
KOI-680b	$0.328^{+0.010}_{-0.009}$	$0.305^{+0.004}_{-0.004}$	$0.353^{+0.012}_{-0.010}$	$0.242^{+0.004}_{-0.006}$	$0.451^{+0.005}_{-0.003}$	$0.207^{+0.001}_{-0.002}$	$0.503^{+0.005}_{-0.006}$	$0.128^{+0.006}_{-0.004}$

very effective at better describing the observations, especially if the ATLAS model intensity profiles are used as inputs. It is interesting to note that the errors given by MC-SPAM are always dominated by the errors on the stellar parameters; this fact is especially evident for Kepler-77, whose uncertainty in the microturbulent velocity of $\pm 0.3 \text{ km s}^{-1}$ leads to larger error bars on the results using the ATLAS models. This highlights the importance of estimating this parameter directly from spectroscopic measurements.

From the sample of low precision LDCs, which is also the cooler star sample (upper panels of Figs 8 and 9), one can see that, without taking into account Kepler-296e, the agreement with the data is very good for ATLAS and PHOENIX model atmospheres for the u_1 coefficients, which shows a mean difference of $-0.046^{+0.133}_{-0.143}$ if one uses the ATLAS models and $-0.049^{+0.138}_{-0.140}$ if one uses the PHOENIX models, both of which are consistent with a zero mean difference. There is a barely significant offset of the u_2 coefficients (2.8σ for the ATLAS models, 2.9σ for the PHOENIX models), with the model values apparently systematically overestimating those coefficients by a mean value of ~ 0.3 . For the sample of high precision LDCs, which is also the hotter star sample (lower panels in those figures), the agreement of the u_1 coefficients is very good for the ATLAS models, with a mean difference of $-0.008^{+0.012}_{-0.012}$ which is consistent with zero, but poor for the PHOENIX models, whose mean difference is $0.083^{+0.008}_{-0.008}$, inconsistent with zero by more than 10σ . Note that this bias is very evident and more prominent for stars hotter than 6000 K, where the model values overestimate the LDCs by ~ 0.1 . For the u_2 coefficients, both model atmospheres show slightly significant biases, with the PHOENIX models doing a better job at predicting the observed LDCs with a mean difference of $-0.024^{+0.012}_{-0.011}$, which is 2σ away from zero, and with the ATLAS models showing a mean difference of $0.042^{+0.012}_{-0.011}$, which is 3.8σ away from zero.

As a final note, there is one particular object worth discussing in detail, Kepler-296e, which has LDCs which deviate more than 2σ

from those of systems with host stars of similar stellar parameters, including Kepler-296f, which according to Torres et al. (2015) orbits the same host star in an orbit almost two times farther away from it. As we can see in Figs 8 and 9, the coefficient changes induced in Kepler-296e due to the geometry of the transit are not expected to be very different from those of Kepler-296f, so the geometry of the system cannot explain the differences on the observed LDCs. Activity could, in principle, produce significant biases on the LDCs through uninoculated spots (Csizmadia et al. 2013), but it seems unlikely that activity affected only one of the observed transits. Because Kepler-296 is known to be a tight binary (Lissauer et al. 2014), one might be tempted to think that Kepler-296e maybe did not orbit the same star as Kepler-296f as claimed by Torres et al. (2015), but its companion. However, both of the stars in the system have actually very similar spectral types and, thus, very similar LDCs, which implies that the observed LDCs are actually very different compared to *both* stars in the system. An analysis of other alternative hypotheses is out of the scope of this work, but we note that these are the kind of analyses that can be performed from measuring, comparing and interpreting LDCs from transit light curves using our MC-SPAM algorithm.

4 THE EFFECT OF USING FIXED LDCS IN TRANSIT FITTING

In the past section, we showed that, as first noted by Howarth (2011), LDCs extracted from fits to intensity profiles of stellar model atmospheres (u_1, u_2) are not directly comparable to the LDCs obtained from transit photometry (u_1^f, u_2^f). This is due to the fact that the two optimization procedures are significantly different from one another and, thus, a geometry-dependent mapping using synthetic light curves has to be carried out in order to obtain the coefficients (u_1^*, u_2^*) that can then be compared to the observed LDCs. This

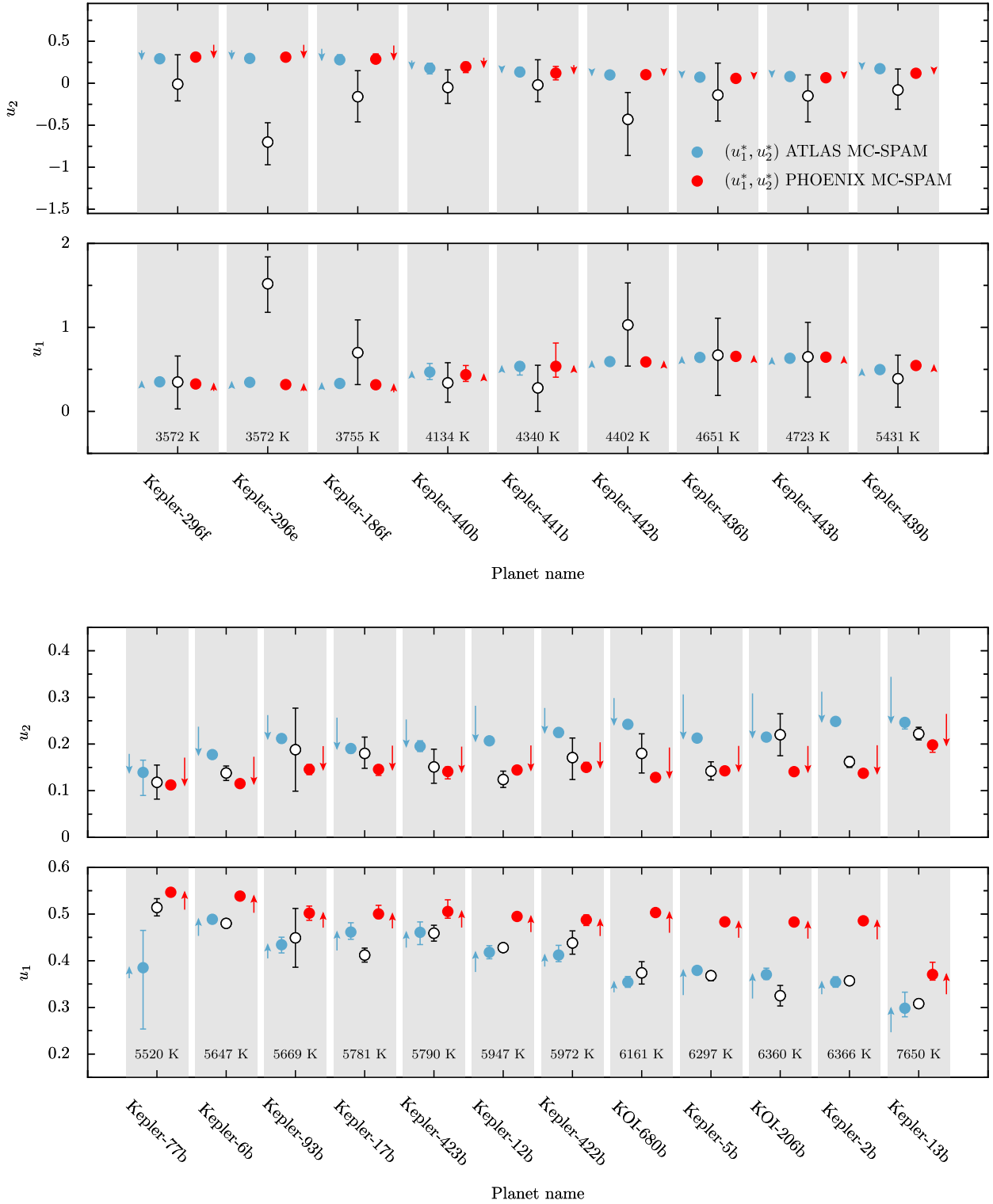


Figure 8. High (bottom panels) and low (upper panels) precision quadratic LDCs derived from transit photometry for several exoplanets (white data points) and MC-SPAM model LDCs (u_1^* , u_2^*) using ATLAS (blue, to the left of each data point) and PHOENIX (red, to the right of each data point) models. The blue and red arrows next to the MC-SPAM results represent the mapping $u_i \rightarrow u_i^*$, i.e. from the original model LDCs obtained from fits to the intensity profiles (in practice obtained using the non-linear coefficients through equation 3) and our MC-SPAM estimates. The temperature of the host star of each system is indicated above each of the planet names, inside the figures. Note the change in scale between the upper and lower panels.

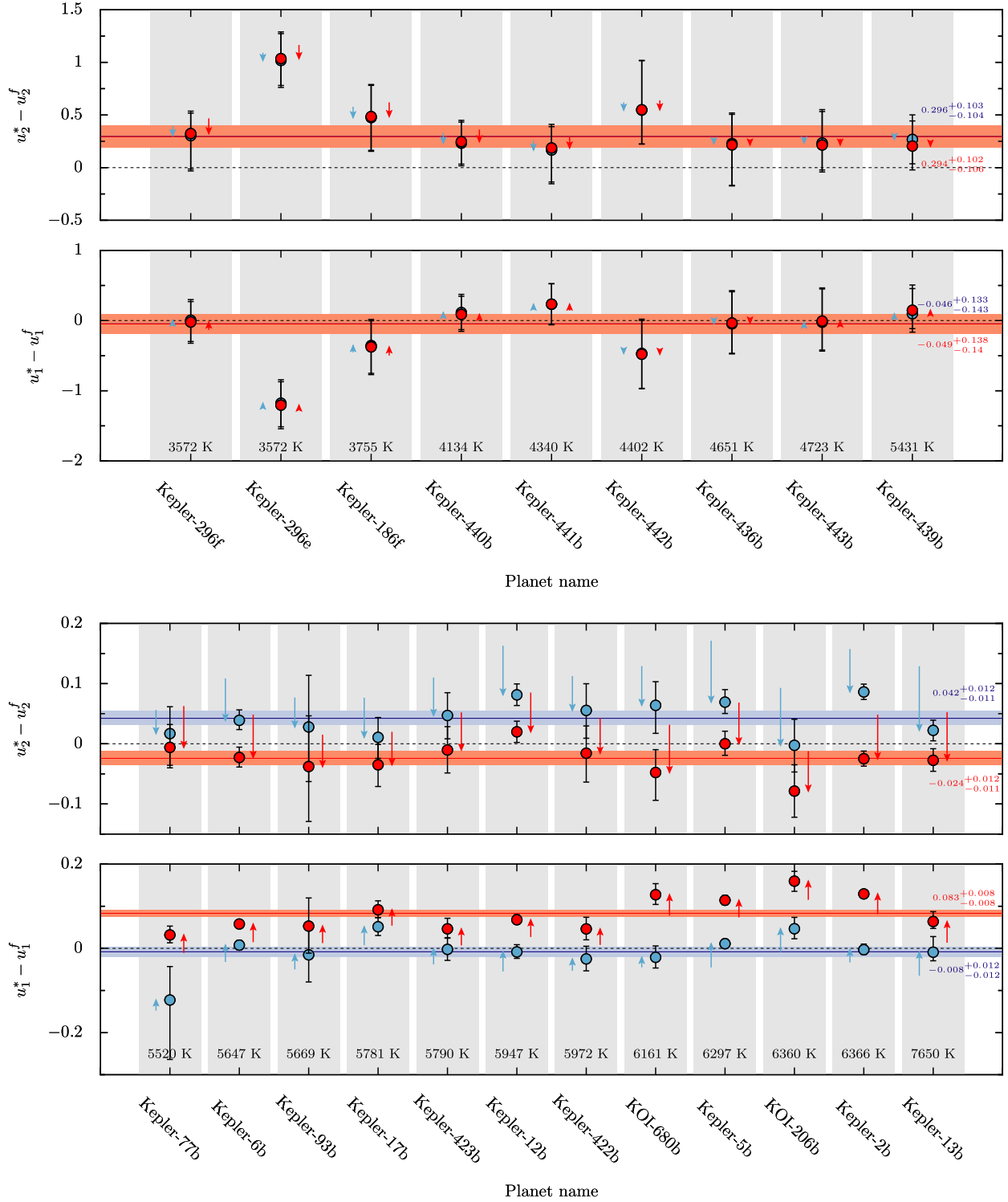


Figure 9. Differences between the observed LDCs (u_1^f, u_2^f) shown in Fig. 8 as white data points and the MC-SPAM estimates (u_1^*, u_2^*) using the ATLAS (blue) and PHOENIX (red) models, which are the blue and red points next to the white data points in Fig. 8. The arrows represent the effect of the MC-SPAM algorithm in the observed difference between (u_1^f, u_2^f) and the original model LDCs obtained from fits to the intensity profiles. The blue bands indicate the 68 per cent bands around the mean of the differences using the ATLAS results (with the median of this indicated by the blue solid line), while the red bands show the same for the PHOENIX models (with the red solid line indicating the median of this distribution). These medians and the associated 68 per cent values are also indicated next to each band (note that in the upper panels both bands overlap). The dashed black line marks zero, for reference.

implies that even if one could measure with excellent precision the intensity profile of a given star, obtain its LDCs with that profile, and then measure those coefficients from transit photometry, also with excellent precision, there is an expected bias between the two sets of coefficients. This in turn means that if one fixes the LDCs obtained from the intensity profile in the transit fitting procedure, then one is using potentially biased coefficients that can then lead to biased transit parameters.¹¹ A strategy to avoid this bias could be to let the LDCs as free parameters in the fit. However, we also expect a bias on the transit parameters in this case if, as it is usually done, the intensity profile is modelled with a quadratic law which we have seen is not able to accurately describe the full intensity profiles.

In addition to the above mentioned problems, there is the issue related to our imperfect knowledge of the underlying, ‘true’, intensity profile. As we saw in Section 3, this is currently an issue as our models are not able to reproduce the observed LDCs with sufficient accuracy. On top of this, according to our results in Section 2, there are differences even between our own modelling of those profiles both between different model atmospheres and between the different methods used to derive the LDCs from them.

In order to explore these sources of bias, in this section we perform simulations to study the possible biases introduced by our limb darkening assumptions on the retrieved transit parameters, using transit light curves generated with the formalism of Mandel & Agol (2002).

4.1 A simulation study

In order to explore the effect on the retrieved transit parameters of fixing or having the LDCs as free parameters, we simulate transit light curves with unit period, circular orbits and an assumed intensity distribution for the host star of the transiting planet. The choice of units such that $P = 1$ is just for convenience of sampling directly in phase and has no consequences for what follows. The geometric parameters of the transit we can retrieve from our simulated light curves are the planet-to-star radius ratio, $p = R_p/R_*$, the semimajor axis to stellar radius ratio, $a_R = a/R_*$, and the inclination of the orbit, i . The simulations were performed as follows. First, based on the data from all transiting planets discovered to date, we choose to generate synthetic transit light curves for planets with all the combinations of parameters $\{a_R, p\}$ with values $a_R = \{3.27, 3.92, 4.87, 6.45, 9.52, 18.18, 200\}$ and $p = \{0.01, 0.06, 0.11, 0.16, 0.21\}$. In order to explore the effect of different impact parameters, $b = \cos(i)a_R$, we also varied b from 0 to 0.9 in steps of 0.1. This defines 350 different orbital configurations for our simulations. For each orbital configuration, we simulated 100 noiseless, uniformly sampled light curves with 1000 in-transit points and 400 out-of-transit points each, whose initial times were randomly perturbed. We first assume perfect knowledge of the underlying intensity profile by generating the transits using the non-linear law with the coefficients $\{c_1, c_2, c_3, c_4\}$ obtained in Section 2 for models with $\log g = 4.5$, solar metallicity, $v_{\text{turb}} = 2 \text{ km s}^{-1}$ and effective temperatures between 3500 and 9000 K. We use the *ATLAS* models, the fitting method of CB11 and the *Kepler* bandpass. Once we generate a simulated light curve, we retrieve its transit geometric parameters using constrained non-linear least-squares with the Levenberg–Marquardt algorithm

using the *LMFIT* package.¹² We perform the fit in two ways: (1) fixing the LDCs to the ones given by the quadratic law for the given star (using the limiting coefficients defined in Section 2); and (2) leaving the LDCs as free parameters in the fit. In the latter case, we fit for the parameters $q_1 = (u_1 + u_2)^2$ and $q_2 = u_1/2(u_1 + u_2)$, where the parameters q_1 and q_2 are constrained to be in (0, 1), in order to obtain physically sound solutions in our non-linear least-square fits (Kipping 2013). For each combination of the geometrical parameters, the median of the fitted parameters obtained from the 100 generated light curves, along with the corresponding errors, is reported.

4.2 The case of central transits

Fig. 10 shows the results of our simulations for the simplest case of a central transit, where the percentual bias induced on p and a_R is shown as a function of the effective temperature of the host star used to extract the LDCs; the upper panel shows the bias induced when fixing the LDCs to model values, and the lower panel shows the bias induced when letting those be free parameters in the optimization procedure (the retrieved inclinations in this case were not reported as they all arrived at the input values). The sizes and colours of the points represent the input values of p and a_R , respectively, with smaller, bluer points representing the lower values of both p and a_R ($p = 0.01$, $a_R = 3.27$), and big, red points representing the highest input values of those parameters ($p = 0.21$, $a_R = 200$). Note that the error bars are plotted, but are smaller than the smallest points in the plot. Note also that some points overlap.

We infer from our simulations that the biases are small for central transits (maximum of ~ 0.2 per cent on p in the case of fitting for the coefficients, ~ -0.05 per cent when fixing them), although significant for several exoplanets: from a query done to the NASA Exoplanet Archive,¹³ 326 Kepler Objects of Interest (KOIs) have quoted uncertainties on p lower than 0.2 per cent and for which the effects of this bias are important. Of those systems 57 are confirmed exoplanets and 113 show quoted uncertainties lower than 0.05 per cent (22 of which are confirmed exoplanets). It is interesting to note that the bias seems to be more important for deeper transits (bigger points in the figure), and the effect is to retrieve deeper transits and larger distances to the host star when fitting for the coefficients, while the opposite effect is introduced when fixing the coefficients, estimating slightly shallower transits and smaller distances to the host star than the real ones. Furthermore, the bias is clearly larger when fitting for the coefficients than when fixing them, which suggests that, if the underlying limb darkening model is accurate at a higher level than the error made by fitting the coefficients, then the best strategy is fixing the LDCs to their model values.

We note that the shape that the biases have as a function of effective temperature are very similar between the different strategies employed to fit the transit light curves. For the *Kepler* bandpass, the difference between the u_i (LDCs obtained from model intensity profiles) and the u_i^* (same coefficients recovered from transit fitting) observed in our experiment in the introduction of Section 3 (Fig. 7) follows a similar shape with temperature as that observed for the biases, that is, starting at the cooler temperatures the offset is larger, decreasing until it reaches a minimum offset at $T_{\text{eff}} = 4750 \text{ K}$, then gradually increasing again for hotter host stars, slightly decreasing

¹¹ The level of bias will depend, among other factors, on the bandpass. In particular, issues noted in this paper should in general be less severe in the infrared.

¹² <http://cars9.uchicago.edu/software/python/lmfit/>

¹³ Query done on 2015 January 25.

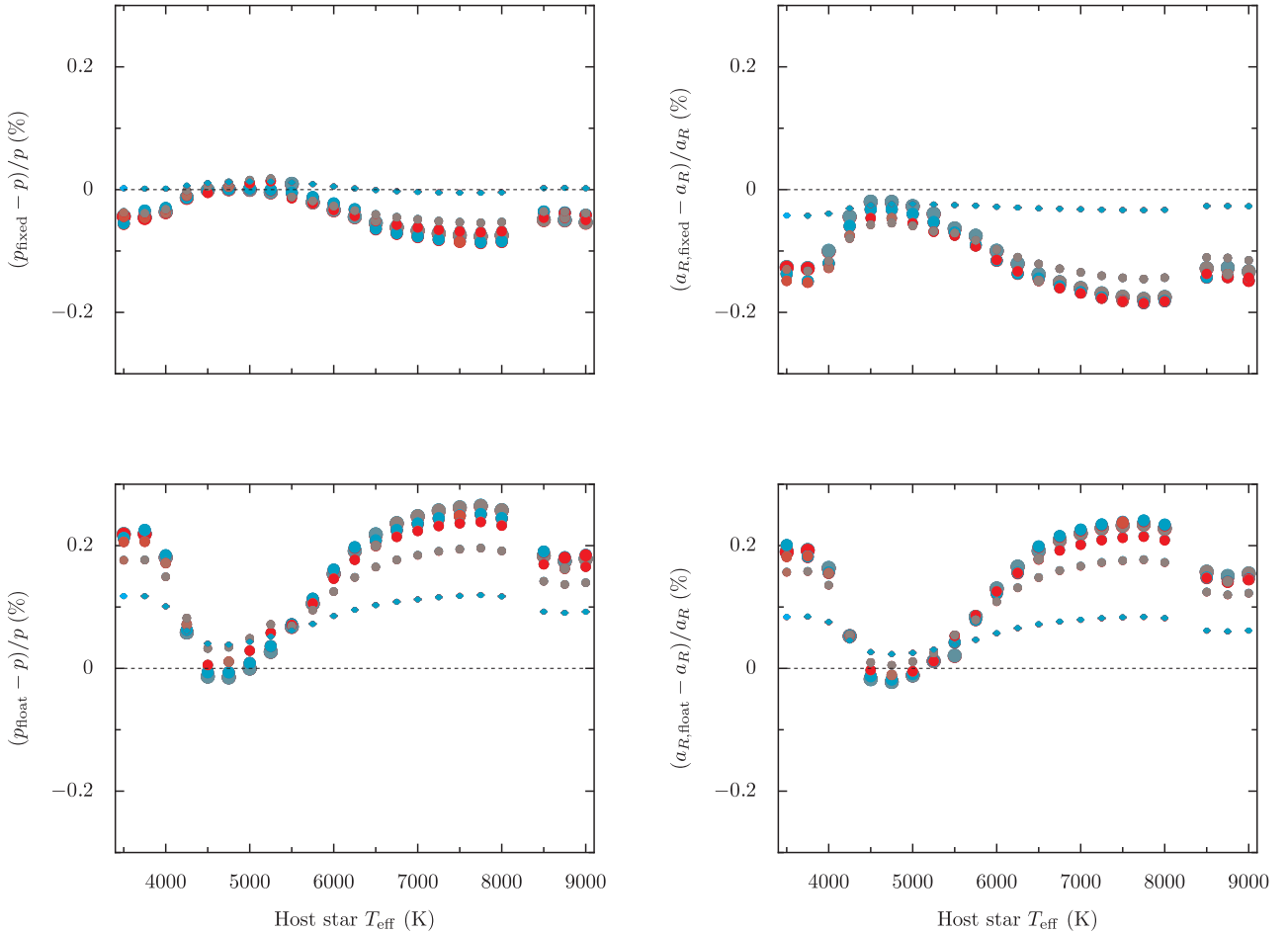


Figure 10. Biases in the recovered planet to star radius ratio $p = R_p/R_*$ and the semimajor axis to stellar radius ratio $a_R = a/R_*$ as a function of temperature obtained from the simulations described in the text. The upper panels show results when fixing the LDCs, while the lower panels show the results when letting them to float in the transit light-curve fit. The size of the points denotes the input value of p ($p = 0.01$, small points; $p = 0.21$, big points), while the colour of the points represents the input value of a_R ($a_R = 3.27$, blue points; $a_R = 200$ red points).

around $T_{\text{eff}} = 8500$ K. This means that the actual mapping $u_i \rightarrow u_i^*$ is less severe for temperatures around $T_{\text{eff}} = 4750$ K, which is one of the reasons why we observe a smaller bias in the retrieved transit parameters around those temperatures in our experiments. Additionally, the performance of the quadratic law fit is also optimal around $T_{\text{eff}} = 4750$ K for this particular bandpass, becoming slightly worse for cooler and hotter stars, a fact already discussed in Section 2.1.2 (Fig. 3). The two points above serve to explain the observed shape of the biases with temperature and in particular the observed minimum of the biases at $T_{\text{eff}} = 4750$ K.

4.3 The case of low and high impact parameter transits

Figs 11 and 12 show the results of our simulations for the cases of low ($b = 0.3$) and high ($b = 0.8$) impact parameters. We can see that the value of b strongly affects the observed bias in the retrieved transit parameters, showing biases as large as ~ 1 per cent for p , and ~ 2 per cent for a_R and i . These biases are larger than for the case of central transits and, therefore, more important. A query to the NASA Exoplanet Archive returns 933 KOIs with uncertainties better than 1 per cent on p , 164 of which are confirmed exoplanets. Furthermore, the impact parameter not only modifies the order of magnitude of the observed bias, but also modifies the trends observed in the case of central transits. For example, in this case, the effect is

more important for shallow transits than for deep transits at most temperatures.

One very interesting fact about our simulations is that although for low impact parameters the bias seems to be larger for a_R and i when fitting for the LDCs, for high impact parameters this effect is reversed, showing higher biases in those parameters when fixing the coefficients. The same effect can be seen for the bias in p in the case of small planets around low-temperature stellar hosts. This is in agreement with the results of Howarth (2011), who showed that the difference between LDCs obtained from model atmospheres and the ones obtained from transit photometry increases as one increases the impact parameter of the transit. This implies that the fixed LDC strategy should worsen as one increases the impact parameter, which is what we observe in our simulations. Therefore, for high impact parameter transits one should fit for the LDCs if one is interested in decreasing the bias, which contrasts with the suggestion of Müller et al. (2013) of fixing them for high impact parameter transits based on the observed increased uncertainty in the retrieved transit parameters when fitting for the coefficients. In our view, the best strategy strongly depends on the quality of the photometry and the observed geometry: if the retrieved uncertainties when fixing the coefficients are smaller than the biases shown here, then the best strategy should be to let the coefficients be free parameters.

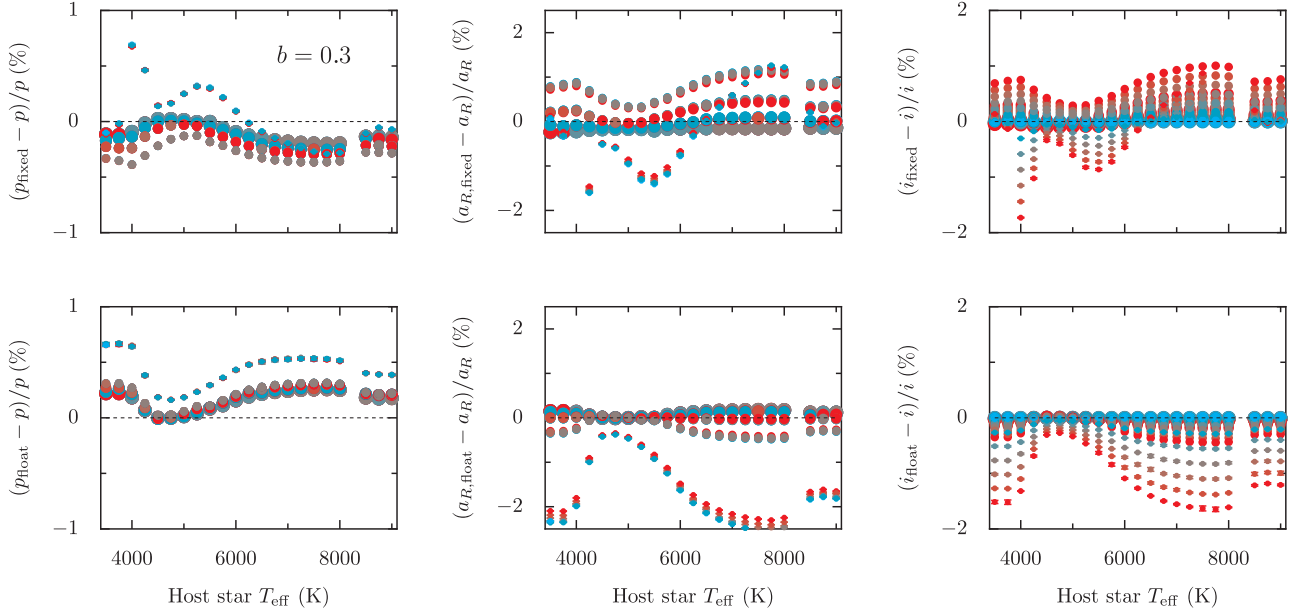


Figure 11. Same as Fig. 10, but with an impact parameter of 0.3 and an additional panel showing the bias induced on inclination i . Note that the scale is different than that of Fig. 10.

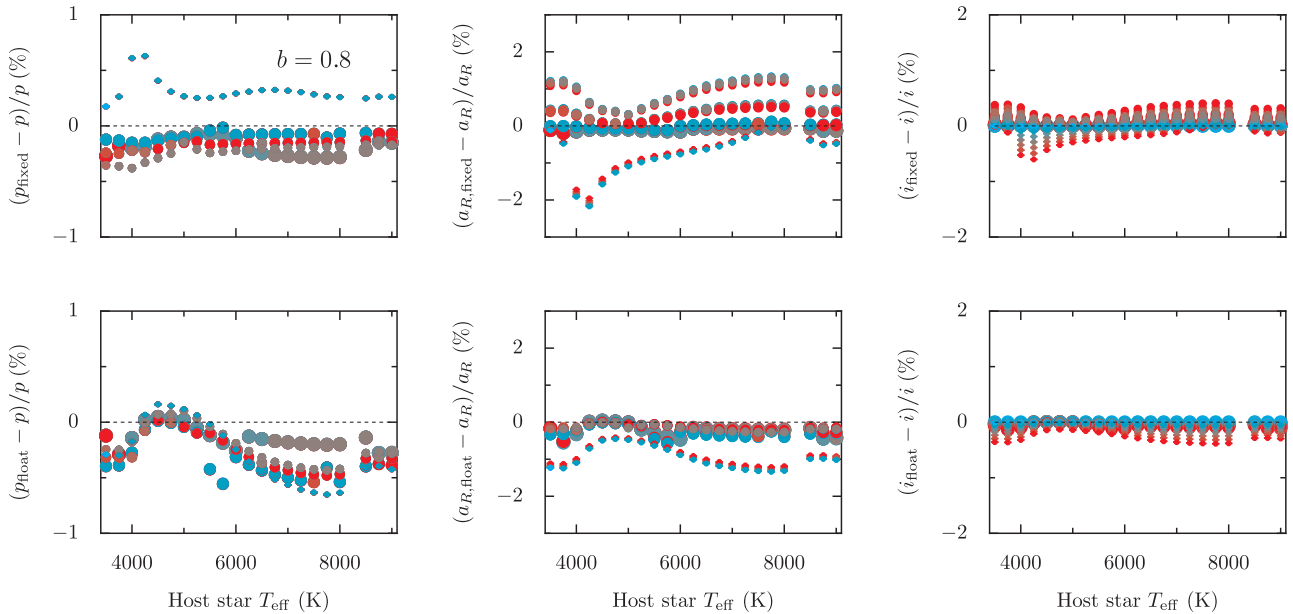


Figure 12. Same as Fig. 11, but with an impact parameter of 0.8. Note that the scale is different than that of Fig. 10, but the same as that of Fig. 11.

4.4 The effect of an unknown stellar intensity profile

In order to explore deviations from the known intensity profile, we make use of previously published LDCs in order to simulate systematic offsets from the limb darkening profile being modelled. To this end, we used the same transit light curves generated in the past subsections, generated with our non-linear LDCs, but fitted them fixing the LDCs to the values published by CB11. In this way, we can explore the impact that different methods for obtaining the LDCs can have on the retrieved transit parameters which, we note, are only lower limits on the actual offsets between the modelled and real profiles, as both using our LDCs or the ones published by CB11 in our analysis in Section 3.2 lead to offsets between observed and

modelled LDCs of the same order. Figs 13 and 14 show the results of our experiments.

As can be seen from our results, the biases follow a similar shape to the difference of the observed quadratic LDCs between our work and that of CB11 in Fig. 2; that is, as expected, the biases are larger where the calculated LDCs show the largest differences. Also, the effect is again more pronounced for smaller values of p , with maximum biases on the order of 3 per cent for planets around stars with $T_{\text{eff}} = 4000$ K with moderate impact parameters ($b = 0.3$), temperature and geometry at which we also observe biases on a_R on the order of ~ 10 per cent, as well as biases on the order of 5 per cent on i . A query to the

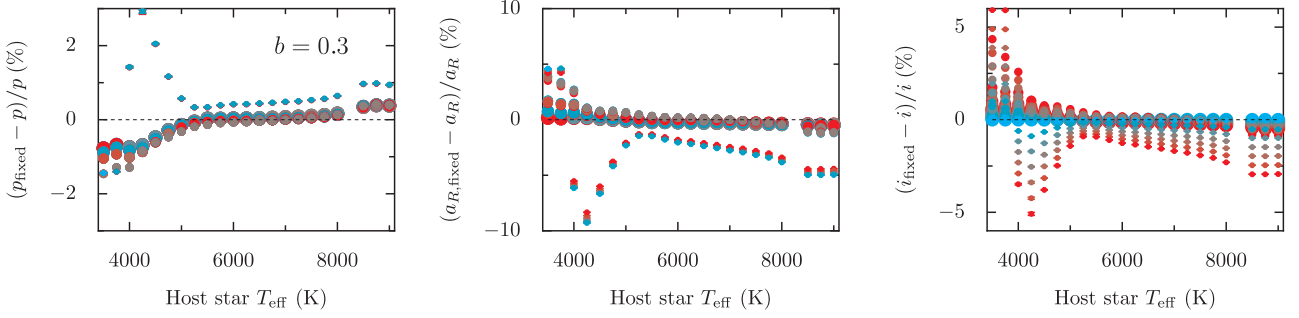


Figure 13. Same as Fig. 10, but with an impact parameter of 0.3 and using LDCs obtained from a different intensity profile (obtained from the work of CB11) to the underlying one (generated using non-linear LDCs from this work). Note that the scale is different from that of previous figures.

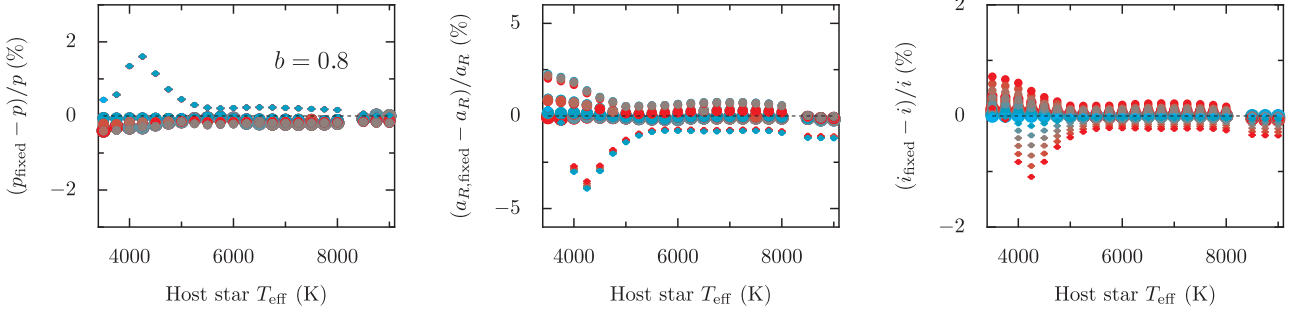


Figure 14. Same as Fig. 13, but with an impact parameter of 0.8. Note that the scale between that figure and this one is also different.

NASA Exoplanet Archive returns 2221 KOIs with uncertainties better than 3 per cent on p , 491 of which are confirmed exoplanets. This is a clear illustration of the importance of our limb darkening assumptions.

5 DISCUSSION

5.1 Lessons learned from the comparison of model-to-observed LDCs

In Section 3, we compared observed LDCs to model LDCs using our new MC-SPAM algorithm, which not only takes into account the geometry of the transit, but also the uncertainties in the transit and host star parameters. From these results, it was apparent that overall the MC-SPAM results using the ATLAS models do a better job at predicting the observed u_1 LDCs for hotter stars than the PHOENIX models, with the tables slightly turned in the case of the u_2 coefficients. Both models seem to do a good job at predicting the u_1 coefficients of cool stars, while slightly overestimating their u_2 coefficients. These results suggest that the non-linear law in general seems unable to predict the limb darkening effect with the accuracy necessary given the quality of available data and, because this is the best representation that we have for the ATLAS and PHOENIX model atmospheres, this suggests that those models are still not reproducing the *observed* limb darkening effect with sufficient accuracy. As such, these model results have to be taken with care and one must be careful in trusting too much the LDCs derived directly from model atmospheres. Our view is that one should always be aware of the possible biases introduced by fixing those coefficients in practical applications.

5.2 Limb darkening and biases in transit parameters: implications for exoplanetary science

The biases uncovered by our experiments in Section 4 are, in general, non-negligible. In particular, the large biases shown for the cases of non-central transits both when assuming a perfectly known intensity profile (Section 4.3) and when assuming deviations from it (Section 4.4) have several implications for exoplanetary science. First, the biases shown for p have a direct impact on population studies that rely on accurate measurements of the planetary radius and their associated uncertainties which, as recently shown by Schlaufman (2015), impact the derived conclusions of these studies. It also has an impact on present and future studies that aim to constrain the interior composition of exoplanets from precise measurements of the planetary radius and mass. For example, Dorn et al. (2015) recently showed that a precision better than ~ 2 per cent on the planetary radius is one of the key ingredients in order to be able to constrain the interior structure of rocky exoplanets. In addition, the biases for a_R have an impact on derived quantities such as the calculated incident fluxes on exoplanets. This parameter, combined with the inclination i of the orbit, defines in turn the impact parameter, which according to our results can vary significantly depending on the different limb darkening assumptions.

5.3 Can the biases be corrected and/or avoided?

As shown in Section 4, the biases introduced by simple parametrizations of the limb darkening effect such as the quadratic law are significant in comparison to the published parameters uncertainties for several confirmed and candidate *Kepler* exoplanets. A natural question to ask is: how can one correct for those biases and how can one avoid them?

The correction of biases in the transit parameters retrieved from a given fit using the quadratic law would necessarily have to involve simulations such as the ones shown here around the parameters of interest. However, an even simpler method would be to fit the original light curve with higher order limb darkening laws like the three-parameter or non-linear laws. The problem with this approach is that, although it seems obvious to switch to higher order laws once the order of magnitude of the bias surpasses the uncertainties in a given parameter, there is always an intrinsic bias on the retrieved transit parameters related to our potentially imperfect knowledge of the exact shape of the underlying intensity profiles in stars which, as shown in Section 4.4, can lead to large biases if the coefficients are fixed in the transit fitting procedure. As shown in Section 3, it appears that better modelling is indeed necessary given that the observed LDCs are not well reproduced by the models. This will be an important endeavour to minimize biases in the parameters estimated from transit light curves, and will be important to fully exploit data from both present high precision missions like *Kepler*, and future high precision missions like the *Transiting Exoplanet Survey Satellite (TESS)* or the *James Webb Space Telescope (JWST)*.

Although a better modelling of stellar atmospheres is an important task, it is also a long-term one. Given the large amount of data already obtained by missions such as *Kepler* and the advent of future missions that will focus on retrieving high precision transit parameters, it is important to discuss short-term strategies that can help overcome the biases due to our limb darkening assumptions shown in this work. The most natural approach would be to fit the transit light curves with high-order laws letting their parameters to float. However, this will most likely be a bad idea for low and medium signal-to-noise ratio light curves due to the degeneracy between the parameters fitted in this procedure. One strategy to overcome this and the problems stated above could be to select a set of high precision transit light curves with precisely known stellar host parameters that have enough signal-to-noise ratio as to be able to be fitted with high-order laws such as the three-parameter or non-linear law. This would in turn allow one to obtain *fitted* LDCs which could then be used to predict or constrain those coefficients for other stars. Although in theory those fitted LDCs are dependent on the transit geometry, this dependence as discussed in Section 3 is rather weak in comparison with the typical uncertainties of the host star parameters and, thus, this strategy seems to be a promising one for achieving high accuracy and precision measurements of transit parameters.

6 CONCLUSIONS

In this paper, we calculated LDCs using the *Kepler* bandpass for both *ATLAS* and *PHOENIX* stellar atmosphere models, and showed that we cannot reproduce previously published values. We could not fully resolve the difference due to the fact the procedures used in the literature are not openly available, but we believe the differences between the different sources of LDCs available in the literature are due to the use of different input model atmospheres. We make our codes available for users to reproduce our results and calculate LDCs for any bandpass in a flexible way.

We showed that different methods used in the fitting stage of the intensity profiles lead to different LDCs. We define a set of quadratic law limiting coefficients that are the best description of the ‘real’ underlying intensity distribution in the sense that they are obtained by sampling uniformly the whole profile. Among previously published methods using the *ATLAS* models, the best is that of [CB11](#) which by generating additional points to the ones directly available from the

models via spline interpolation provides a good approximation to a denser sampling of the underlying profile. We also point out an important correction that needs to be applied when dealing with the spherically symmetric *PHOENIX* models so that the stellar radius definition is consistent with the plane-parallel *ATLAS* models. We provide updated LDCs using *PHOENIX* models with this correction applied which are now directly comparable to those derived using *ATLAS* models.

In order to map model LDCs to those determined by transit photometry we introduce an algorithm called *MC-SPAM*, which builds upon the *SPAM* algorithm proposed by Howarth (2011). The algorithm takes into consideration not only the fact that LDCs obtained from intensity profiles of model stellar atmospheres are not directly comparable to the coefficients estimated from transit photometry, but also the fact that all the stellar parameters and geometrical parameters of the transit have measurement errors. We use *MC-SPAM* to compare LDCs predicted by models for a sample of systems which have had their LDCs determined from *Kepler* transit photometry. We show that the *ATLAS* and *PHOENIX* models are not able to fully reproduce the observed limb darkening effect for systems with a wide range of stellar parameters. Finally, we showed that, when using the quadratic law, fixing and letting the LDCs be free in the transit fitting procedures induce biases on the retrieved transit parameters that are significant for several candidate and confirmed *Kepler* planets, even if one assumes a perfectly known stellar intensity profile.

Given our results, we conclude that if one is confronted with a transit light curve and one decides to use the quadratic limb darkening law to model the limb darkening effect, the best strategy in order to minimize the bias introduced in the transit parameters is to let them float in the transit fitting procedure. Although a natural strategy to follow once the biases introduced by a given limb darkening law are important for a given system geometry and precision would be to switch to higher order laws, one has to be careful if the strategy is to fix the LDCs. This is because the strategy would also lead to an underlying bias due to our still incomplete knowledge of the intensity distribution of real stars; *our understanding of stellar model atmospheres is not good enough to avoid biases by switching to using fixed model coefficients from higher order laws*. As a short-term solution to this problem, we propose to fit a set of high signal-to-noise ratio light curves with precisely known stellar host parameters using a high-order law parametrization such as the three-parameter or non-linear laws in order to obtain the LDCs directly from data, which could then be used to predict or at least constrain the values of those coefficients for other exoplanetary systems.

The results shown in this work imply that the current achievable *precision* is smaller than the current achievable *accuracy* if one considers only our limb darkening assumptions. Because of this, we call the attention to observers to be careful about their limb darkening assumptions, and suggest always leaving room for flexibility on the LDCs in the transit fitting procedures even when fitting high-order laws in order to shield against biases in the retrieved transit parameters. If precision is more important than accuracy (e.g. in applications such as transmission spectroscopy), we suggest performing simulations similar to the ones shown in this work in order to quantify the order of magnitude of any biases if the choice is to leave the LDCs fixed.

ACKNOWLEDGEMENTS

NE is supported by CONICYT-PCHA/Doctorado Nacional. NE and AJ acknowledge support from the Ministry for the Economy, Development, and Tourism’s Programa Iniciativa Científica Milenio

through grant IC 120009, awarded to the Millennium Institute of Astrophysics (MAS). AJ acknowledges support from FONDECYT project 1130857 and from BASAL CATA PFB-06. We would like to thank the anonymous referee for helpful comments, questions and suggestions that helped to improve this work. We would also like to thank Pierre Kervella and Antoine Mérand who pointed out to us the fact that PHOENIX models have a limb definition inconsistent with that of plane-parallel ATLAS models, Benjamin Rackham for his assistance on writing initial versions of the fitting procedures for the PHOENIX models, Antonio Claret, David Sing and Tom Evans for useful discussions regarding the procedures they used for obtaining LDCs and Ashley Villar, Jontahan Fraine, Amaury Triaud and Rafael Brahm for useful discussions regarding the results of this paper.

Some of the data presented in this paper were obtained from the Mikulski Archive for Space Telescopes (MAST). STScI is operated by the Association of Universities for Research in Astronomy, Inc., under NASA contract NAS5-26555. Support for MAST for non-HST data is provided by the NASA Office of Space Science via grant NNX13AC07G and by other grants and contracts. This paper includes data collected by the *Kepler* mission. Funding for the *Kepler* mission is provided by the NASA Science Mission directorate.

REFERENCES

- Abubekrov M. K., Gostev N. Yu., 2013, MNRAS, 432, 2216
 Almenara J. M. et al., 2015, A&A, 575, A71
 Aufdenberg J. P., Ludwig H.-G., Kervella P., 2005, ApJ, 633, 424
 Azzalini A., 1985, Scandinavian J. Stat., 12, 171
 Ballard S. et al., 2014, ApJ, 790, 12
 Bonomo A. et al., 2012, A&A, 538, A96
 Claret A., 2000, A&A, 363, 1081
 Claret A., Bloemen S., 2011, A&A, 529, A75 (CB11)
 Claret A., Hauschildt P. H., 2003, A&A, 412, 241
 Claret A., Hauschildt P. H., Witte S., 2012, A&A, 546, A14 (CHW)
 Claret A., Hauschildt P. H., Witte S., 2013, A&A, 552, A16 (CHW)
 Csizmadia Sz., Pasternacki Th., Dreyer C., Cabrera J., Erikson A., Rauer H., 2013, A&A, 549, A9
 Díaz-Cordovéz J., Giménez A., 1992, A&A, 259, 227
 Dorn C., Khan A., Heng K., Alibert Y., Connolly J., Benz W., Tackley P., 2015, preprint (arXiv:1502.03605)
 Dunham E. W. et al., 2010, ApJL, 713, 136
 Eastman J., Gaudi B. S., Agol E., 2013, PASP, 125, 83
 Endl M. et al., 2014, ApJ, 795, 151
 Fortney J. J. et al., 2011, ApJS, 197, 9
 Fraine J. et al., 2014, Nature, 513, 526
 Gandolfi D. et al., 2013, A&A, 557, A74
 Hébrard G. et al., 2014, A&A, 572, A93
 Howarth I. D., 2011, MNRAS, 418, 1165
 Howell S. et al., 2010, ApJ, 725, 1633
 Husser T.-O., Wende-von Berg S., Dreizler S., Homeier D., Reiners A., Barman T., Hauschildt P. H., 2013, A&A, 553, A6
 Kipping D. M., 2013, MNRAS, 435, 2152
 Kjurkchieva D., Dimitrov D., Vladav A., Yotov V., 2013, MNRAS, 431, 3654
 Klimesmith D. A., Sobieski S., 1970, AJ, 75, 175
 Koch D. G. et al., 2010, ApJ, 713, L131
 Kurucz R. L., 1979, ApJS, 40, 1
 Lissauer J. J. et al., 2014, ApJ, 784, 44
 Lund M. et al., 2014, A&A, 570, A54
 Mandel K., Agol E., 2002, ApJ, 580, L171
 Müller H. M., Huber K. F., Czesla S., Wolter U., Schmitt J. H. M. M., 2013, A&A, 560, A112
 Neilson H. R., Lester J. B., 2013a, A&A, 554, A98
 Neilson H. R., Lester J. B., 2013b, A&A, 556, A86
 Plez B., 2011, J. Phys.: Conf. Ser., 328, 012005
 Schlaufman K., 2015, ApJ, 799, L26
 Shporer A. et al., 2014, ApJ, 788, 92
 Sing D. K., 2010, A&A, 510, A21 (S10)
 Sing D. K., Désert J.-M., Lecavelier Des Etangs A., Ballester G. E., Vidal-Madjar A., Parmentier V., Hébrard G., Henry G. W., 2009, A&A, 505, 891
 Torres G. et al., 2015, ApJ, 800, 99
 Wittkowski M., Aufdenberg J. P., Kervella P., 2004, A&A, 413, 711

APPENDIX A: LEAST-SQUARES FITS TO LIMB-DARKENING LAWS

Fits of stellar model atmosphere intensities with the laws mentioned in the Introduction require a least-squares procedure to be followed which, in general, minimizes the quantity

$$\chi^2 = \sum_{i=1}^N w_i (y_i - f(x_i))^2, \quad (\text{A1})$$

where y_i are the data points to be fitted, $f(x_i)$ the model for those data points, w_i the weight given to each squared residual $(y_i - f(x_i))^2$ and N the number of data points to be fitted. In our case we set $w_i = 1$ and the objective is to minimize equation (A1) using the various models presented in the Introduction of this work.

If no constraint is provided, then the problem is easily solved for all the laws presented because the coefficients which make up each law in the parameters. Our objective then is to minimize equation (A1) with $y_i = I(\mu_i)/I(1)$, and $x_i = \mu_i$ (the angles at which each of those integrations are done), for the different models $f(\mu_i)$ presented in the Introduction, obtaining the optimal coefficients in a least-squares sense. The models have the form

$$f(\mu_i) = 1 - \sum_n \theta_n g_n(\mu_i),$$

where θ_n are the parameters of the laws (e.g. $\theta_n = c_n$ for the non-linear law) and $g_n(\mu_i)$ are the functions which make up each law, e.g. in the case of the non-linear law (which contains the linear, square-root and three-parameter laws depending on which coefficient θ_n one sets to zero), $g_n(\mu_i) = (1 - \mu_i^{n/2})$. In order to minimize equation (A1), we calculate the partial derivatives of χ^2 with respect to the different coefficients θ_n and set them to zero. The calculation is easily found to give

$$\frac{\partial \chi^2}{\partial \theta_k} = \sum_{i=1}^N 2(f(\mu_i) - I(\mu_i)/I(1)) \frac{\partial f(\mu_i)}{\partial \theta_k} = 0,$$

with

$$\frac{\partial f(\mu_i)}{\partial \theta_k} = -g_k(\mu_i),$$

which, after rearranging terms, gives the system of k linear equations for the n coefficients θ_n :

$$\sum_n \theta_n \alpha_{n,k} = \beta_k, \quad k = 1, 2, \dots, n,$$

with

$$\alpha_{n,k} = \sum_{i=1}^N g_n(\mu_i) g_k(\mu_i),$$

$$\beta_k = \sum_{i=1}^N g_k(\mu_i) (1 - I(\mu_i)/I(1)),$$

which are trivial to solve. Note also that if we write the linear system as $\mathbf{A}\boldsymbol{\theta} = \mathbf{b}$, with $\mathbf{A}_{n,k} = \alpha_{n,k}$, $\boldsymbol{\theta} = \{\theta_1, \theta_2, \dots, \theta_n\}^T$ and

$\mathbf{b} = \{\beta_1, \beta_2, \dots, \beta_n\}^T$, in this case the matrix \mathbf{A} is symmetric, so the system is not only linear but very fast to compute. As an example of how to use the above result, for the linear law the only function is $g_1(\mu_i) = 1 - \mu_i$ so, in this case, there is only one equation for the parameter $\theta_1 = a$ with parameters

$$\alpha_{1,1} = \sum_{i=1}^N (1 - \mu_i)^2,$$

$$\beta_1 = \sum_{i=1}^N (1 - \mu_i)(1 - I(\mu_i)/I(1)),$$

which gives

$$\theta_1 = a = \frac{\beta_1}{\alpha_{1,1}} = \frac{\sum_{i=1}^N (1 - \mu_i)(1 - I(\mu_i)/I(1))}{\sum_{i=1}^N (1 - \mu_i)^2}. \quad (\text{A2})$$

APPENDIX B: LIMITING CASES FOR KNOWN TARGET LIMB-DARKENING LAWS

If we try to fit an arbitrary law when knowing that we are sampling from a law of the form $I(\mu_i)/I(1)$ (e.g. the non-linear law), then ‘limiting coefficients’ corresponding to $N \rightarrow \infty$ can be obtained. To perform this calculation, we sample N uniform μ_i points by defining $\mu_i = (i - 1)/(N - 1)$, with $i = 1, 2, \dots, N$ (note that this samples μ_i angles from $\mu_i = 1$ for $i = N$ to $\mu_i = 0$ for $i = 1$). We introduce this sampling sums that give the parameters (e.g. equation A2 for the parameter of the linear law) and then take the limit as $N \rightarrow \infty$.

B1 Limiting coefficient a for the linear law when sampling from the non-linear law

We sample N intensity ($I(\mu_i)/I(1)$) and angle (μ_i) pairs from the non-linear law, i.e.

$$I(\mu_i)/I(1) = 1 - \sum_{n=1}^4 c_n (1 - \mu_i^{n/2}),$$

with known coefficients c_n . We now fit the profile with a linear law and determine the limiting coefficient a that follows as $N \rightarrow \infty$. We first find the numerator and the denominator in equation (A2). The denominator is easily found to be

$$\sum_{i=1}^N (1 - \mu_i)^2 = \frac{2N^2 - N}{6(N - 1)} = h(N),$$

while the numerator takes the form

$$\sum_{i=1}^N (1 - \mu_i)(1 - I(\mu_i)/I(1)) = \sum_{n=1}^4 c_n S_n,$$

with $S_n = \sum_{i=1}^N (1 - \mu_i - \mu_i^{n/2} + \mu_i^{(n+2)/2})$. It is straightforward to show that

$$S_1 = \frac{N}{2} + \sum_{i=1}^N \mu_i^{3/2} - \sum_{i=1}^N \mu_i^{1/2},$$

$$S_2 = \frac{2N^2 - N}{6(N - 1)} = h(N),$$

$$S_3 = \frac{N}{2} + \sum_{i=1}^N \mu_i^{5/2} - \sum_{i=1}^N \mu_i^{3/2},$$

$$S_4 = \frac{5N^2 - 4N}{12(N - 1)},$$

where we have expressed the sums of non-integer powers of μ_i directly. Now equation (A2) reads

$$\theta_1 = a = \frac{\sum_{i=1}^N (1 - \mu_i)(1 - I(\mu_i)/I(1))}{\sum_{i=1}^N (1 - \mu_i)^2} = \sum_{n=1}^4 c_n \frac{S_n}{h(N)},$$

and we need to take the limit as $N \rightarrow \infty$. The main challenge for taking this limit is to obtain a closed form expression for the limit of the ratio between the sums of non-integer powers of μ_i and $h(N)$, terms which appear in the ratios $S_1/h(N)$ and $S_3/h(N)$. To evaluate this, we first obtain an expression for the sums of non-integer powers of μ_i . In order to do so, we note that, for (integer and non-integer) exponent $k \neq \pm 1$,

$$\sum_{i=1}^N \mu_i^k = \frac{1}{(N - 1)^k} \left(\sum_{j=0}^N j^k - N^k \right)$$

$$= \frac{1}{(N - 1)^k} \left(\frac{N^{k+1}}{k+1} - \frac{N^k}{2} + \mathcal{O}(N^{k-1}) \right),$$

where in the last step we have used the Euler–Maclaurin summation formula. This implies that

$$\frac{\sum_{i=1}^N \mu_i^k}{h(N)} = \frac{6(N - 1)^{(1-k)}}{(2N - 1)} \left(\frac{N^k}{k+1} - \frac{N^{k-1}}{2} + \mathcal{O}(N^{k-2}) \right),$$

whose limit as $N \rightarrow \infty$ is easily found as all terms to the right-hand side of the first term in this expression vanish in that limit, i.e.

$$\lim_{N \rightarrow \infty} \frac{\sum_{i=1}^N \mu_i^k}{h(N)} = \lim_{N \rightarrow \infty} \frac{6(N - 1)^{(1-k)}}{(2N - 1)} \left(\frac{N^k}{k+1} \right) = \frac{3}{1+k}.$$

Using this result, we finally find

$$\lim_{N \rightarrow \infty} a = \lim_{N \rightarrow \infty} \sum_{n=1}^4 c_n \frac{S_n}{h(N)} = \frac{7}{10} c_1 + c_2 + \frac{81}{70} c_3 + \frac{5}{4} c_4.$$

B2 Limiting coefficients u_1 and u_2 for the quadratic law when sampling from the non-linear law

Following the results in Appendix A, in the general case of all the two-parameter limb darkening laws there are two equations for the parameters θ_1 and θ_2 , with

$$\theta_1 = \frac{\beta_2 \alpha_{2,1} - \beta_1 \alpha_{2,2}}{\alpha_{1,2} \alpha_{2,1} - \alpha_{1,1} \alpha_{2,2}}, \quad (\text{B1})$$

$$\theta_2 = \frac{\beta_1 \alpha_{1,2} - \beta_2 \alpha_{1,1}}{\alpha_{1,2} \alpha_{2,1} - \alpha_{1,1} \alpha_{2,2}}. \quad (\text{B2})$$

Specializing to the case of the quadratic law (i.e. $\theta_1 = u_1$ and $\theta_2 = u_2$), we obtain

$$\alpha_{n,k} = \sum_{i=1}^N (1 - \mu_i)^{n+k},$$

$$\beta_k = \sum_{i=1}^N (1 - \mu_i)^k (1 - I(\mu_i)/I(1))$$

for $n = 1, 2$ and $k = 1, 2$. We note that in this case $\alpha_{n,k} = \alpha_{k,n}$, with

$$\alpha_{1,1} = \sum_{i=1}^N (1 - \mu_i)^2 = \frac{2N^2 - N}{6(N - 1)},$$

$$\alpha_{1,2} = \sum_{i=1}^N (1 - \mu_i)^3 = \frac{N^2}{4(N - 1)},$$

$$\alpha_{2,2} = \sum_{i=1}^N (1 - \mu_i)^4 = \frac{N(2N-1)(3N^2-3N-1)}{30(N-1)^3},$$

and the β_k are of the form

$$\beta_1 = \sum_{n=1}^4 c_n S_n,$$

$$\beta_2 = \sum_{n=1}^4 c_n B_n,$$

with the S_n given in the past subsection and

$$B_1 = \frac{2N^2 - N}{6(N-1)} + \sum_{i=1}^N 2\mu_i^{3/2} - \mu_i^{5/2} - \mu_i^{1/2},$$

$$B_2 = \frac{N^2}{4(N-1)},$$

$$B_3 = \frac{2N^2 - N}{6(N-1)} + \sum_{i=1}^N 2\mu_i^{5/2} - \mu_i^{7/2} - \mu_i^{3/2},$$

$$B_4 = \frac{9N^4 - 21N^3 + 14N^2 - N}{30(N-1)^3}.$$

The denominator of the expressions for u_1 and u_2 , i.e. the denominator of equations (B1) and (B2), is given by

$$\alpha = \alpha_{1,2}^2 - \alpha_{1,1}\alpha_{2,2} = \frac{(3N^2 - 3N + 2)(N+1)(2-N)N^2}{720(N-1)^4}.$$

We now note that the limits we want to obtain can be written as

$$\lim_{N \rightarrow \infty} u_1 = \lim_{N \rightarrow \infty} \frac{\beta_2 \alpha_{2,1}}{\alpha} - \lim_{N \rightarrow \infty} \frac{\beta_1 \alpha_{2,2}}{\alpha},$$

$$\lim_{N \rightarrow \infty} u_2 = \lim_{N \rightarrow \infty} \frac{\beta_1 \alpha_{1,2}}{\alpha} - \lim_{N \rightarrow \infty} \frac{\beta_2 \alpha_{1,1}}{\alpha},$$

which using the same methods as in Appendix B1 gives

$$\lim_{N \rightarrow \infty} u_1 = \frac{12}{35}c_1 + c_2 + \frac{164}{105}c_3 + 2c_4,$$

$$\lim_{N \rightarrow \infty} u_2 = \frac{10}{21}c_1 - \frac{34}{63}c_3 - c_4.$$

APPENDIX C: FITTING AND SAMPLING FROM SKEW-NORMAL DISTRIBUTIONS GIVEN PARAMETER ESTIMATES WITH ASYMMETRICAL ERROR BARS

Given an estimate of a parameter θ in the form $\hat{\theta}_{-\sigma_2}^{\sigma_1}$, where in general $\sigma_1 \neq \sigma_2$, we want to sample points from the posterior distribution of θ , given the data, only knowing that the distribution is asymmetric. One choice for performing such sampling is to assume that the distribution of θ is a skew-normal distribution with parameters μ , σ and α , which is given by

$$p(\theta|\mu, \sigma, \alpha) = p_\alpha \left(\frac{\theta - \mu}{\sigma} \right) \frac{1}{\sigma},$$

where

$$p_\alpha(y) = 2\phi(y)\Phi(\alpha y)$$

and

$$\phi(y) = \exp(-y^2/2)/\sqrt{2\pi}, \quad \Phi(\alpha y) = \int_{-\infty}^{\alpha y} \phi(t) dt.$$

In this distribution, μ is the mean, σ^2 its variance and α , also called the shape parameter, defines its skewness. Note that when $\alpha = 0$, we recover a normal distribution of mean μ and variance σ^2 .

C1 Fitting a skew-normal distribution to observed estimates

A simple way to obtain the parameters $\{\mu, \sigma, \alpha\}$ of the distribution for each parameter is to assume that $\hat{\theta} - \sigma_2$, $\hat{\theta}$ and $\hat{\theta} + \sigma_1$ define the 0.16, 0.5 and 0.84 quantiles of the parameter distribution (i.e. the quoted value of the parameter defines the median and the errors define the 68 per cent credibility bands around it). We can now easily formulate the problem as a non-linear least-squares problem where the independent, observed, variables are the observed values at the given quantiles (i.e. $\mathbf{x} = \{\hat{\theta} - \sigma_2, \hat{\theta}, \hat{\theta} + \sigma_1\}$) and the dependent variables are the quantiles (i.e. $\mathbf{y} = \{0.16, 0.5, 0.84\}$). Then, we minimize

$$r = \|\mathbf{y} - \mathbf{m}(\mathbf{x}, \mu, \sigma, \alpha)\|,$$

where the i th element of \mathbf{m} is given by

$$m_i = \int_{-\infty}^{x_i} p(\theta|\mu, \sigma, \alpha) d\theta,$$

which can be solved with any non-linear least-squares algorithm such as Levenberg–Marquardt.

C2 Sampling from a skew-normal with known parameters

Once the parameters for a given skew-normal distribution are known, we want to sample values from it in a simple and efficient fashion. The following algorithm has been published by A. Azzalini in his personal webpage,¹⁴ but we quote it here for completeness.

First, one has to compute the parameter $\delta = \alpha/\sqrt{1+\alpha^2}$. With this, one now samples the random variables u_0, v , both of which are independent and have standard normal distributions, and generate the random variable $u_1 = \delta u_0 + \sqrt{1-\delta^2}v$ which has correlation δ with u_0 . Then, sample the random variable z which equals u_1 if $u_0 > 0$ and $-u_1$ otherwise. With this, z has a skew-normal distribution with zero mean, $\sigma = 1$ and shape parameter α . Finally, the random variable $SN = \mu + \sigma z$ has a skew-normal distribution with mean μ , variance σ^2 and shape parameter α .

¹⁴ <http://azzalini.stat.unipd.it/SN/faq-r.html>

This paper has been typeset from a \LaTeX file prepared by the author.